electronics

Review

A Review of Research on Dual-Side Control Methods for Magnetic Coupling Wireless Power Transfer Systems Based on Dual-Active Bridge Converters

Yanwei Jiang, Yingao Li, Jingjing Yang and Xujian Shu *

School of Electrical Engineering and Automation, Fuzhou University, Fuzhou 350108, China; jiang_yanwei@fzu.edu.cn (Y.J.); bingganaoliao@gmail.com (Y.L.); yangjingjing06046@fzu.edu.cn (J.Y.)
* Correspondence: xujian_shu@fzu.edu.cn; Tel.: +86-188-5010-0370

Abstract: Magnetic Coupling Wireless Power Transfer (MCWPT) technology has broad application prospects due to its high degree of freedom in energy exchange and unparalleled security. In recent years, various controllers have been added to WPT systems to improve energy transfer performance. Among them, the Dual-Side Control (DSC) approach, which employs Dual-Active Bridge (DAB) converters with simultaneous control of the transmitter and receiver, has made great progress. The DAB structure has a compromise between cost and complexity, and the DSC can bring a high enough degree of control freedom to the MCWPT system to easily achieve efficiency optimization and desired output characteristics. However, various DSC methods have different characteristics. Therefore, this paper reviews and summarizes the current research status of DSC methods based on the DAB converters in MCWPT systems. Wireless communication is one of the decisive factors in the design of a control strategy, which is categorized in this paper according to the main approaches used in all the papers. Various DSC strategies are described in detail and compared comprehensively according to the control variables and control objectives. This review will be highly beneficial to research entities and industry professionals as a ready reference for the control design in MCWPT.

Keywords: dual-side control strategy; magnetic coupling; wireless power transfer; dual-active bridge converters; wireless communication; constant output; efficiency optimization; high robustness

check for updates

Citation: Jiang, Y.; Li, Y.; Yang, J.; Shu, X. A Review of Research on Dual-Side Control Methods for Magnetic Coupling Wireless Power Transfer Systems Based on Dual-Active Bridge Converters. *Electronics* **2024**, *13*, 4765. https://doi.org/10.3390/electronics13234765

Academic Editor: Djuradj Budimir

Received: 6 November 2024
Revised: 29 November 2024
Accepted: 30 November 2024
Published: 2 December 2024

Copyright: © 2024 by the authors. Licensee MDPI, Basel, Switzerland. This article is an open access article distributed under the terms and conditions of the Creative Commons Attribution (CC BY) license (https://creativecommons.org/licenses/by/4.0/).

1. Introduction

It has long been a dream of humanity to realize the popularity of wireless power transfer technology [1]. There is no physical contact in the energy transmission path of WPT, which avoids the stubborn diseases of traditional wired transmission methods, such as line aging, electrostatic sparks, and contact wear. According to the classification of the transmission medium, WPT can be divided into magnetic field coupling [2,3], electric field coupling [4,5], electromagnetic radiation coupling [6,7], and ultrasonic WPT technology [8]. MCWPT realizes power transmission in the near field through the magnetic field between inductance coils, which has the advantages of medium transmission distance (a few centimeters to a few meters), less dependence on the transmission medium, and high security. Today, MCWPT is widely used in Unmanned Aerial Vehicles (UAVs), Electric Vehicles (EVs) [9,10], mobile phone charging [11], biomedicine [12,13], and other application scenarios.

For practical application scenarios, the equivalent internal resistance of variable loads such as batteries changes during charging, and the position of the coil shifts depending on the demand for powering the device. As a result, the load and mutual inductance will inevitably change, affecting the transmission characteristics of the system. In order to meet the high-quality transmission of electrical energy, the main design objectives of MCWPT can be summarized in three aspects:

1. Constant output;
2. Optimal efficiency;
3. High robustness.

Constant output can be achieved by the design of resonant topologies, including coupling coil winding methods, parameter optimization, etc. The four basic compensation topologies, SS, SP, PP, and PS, are simple in structure but are strongly influenced by mutual inductance. As a result, multiple resonant elements have been used. High-order resonant topologies consisting of LCL or LCC structures have higher parameter design freedom, and when used on the transmitter side, they can make the coil current constant [14] to prevent overcurrent problems during system operation. By combining with LC topologies, they can realize Constant Voltage Output (CVO) or Constant Current Output (CCO) to improve the sensitivity of the system to parameter variations [15,16]. There are also papers devoted to the study of higher-order [17] or combined resonant [18] topology to achieve constant output under variable load and variable coupling, but this undoubtedly increases the complexity of the system, and usually cannot achieve high-precision output. Constant output can also be achieved without complex topology construction using only transmitter-side control (TSC), but it usually requires additional DC/DC converters [19] or wireless communication [20], which leads to higher control complexity even if both are optimized away [21]. In receiver-side control (RSC), constant output does not require wireless communication, and there is no control variable regulation on the transmitter side. Therefore, the RSC scheme with a cascaded DC/DC converter is simple to control [22], but the size and weight of the system is large in comparison to Active Rectifier (AR), which can only simplify the circuit topology; however, the control loop is complex [23]. DSC has been used to achieve a constant output of MCWPT due to its advantages of high control freedom, low complexity requirement of the circuit structure, and high reliability, and more and more methods have been proposed to optimize the transmission characteristics of the system.

The efficiency of MCWPT is affected by the coupling coefficient k and the quality factor Q. Improving the efficiency can be achieved by optimizing the design of the coupling mechanism [24], but the optimal efficiency is usually accompanied by certain loading conditions, and the method is born from this is Impedance Matching (IM). It has been studied that IM can design a capacitance inductance tuning network [25,26], but the increased resonant elements will inevitably produce losses. Whereas the use of control for Maximum Efficiency Point Tracking (MEPT) improves output accuracy and simplifies the circuit topology, TSC optimizes efficiency by controlling the duty cycle, phase shift angle [27], or frequency [28], and RSC enables IM through wireless communication [29]; however, this is limited by the difficulty of achieving multiple control objectives due to the degrees of freedom of the control, which results in a decrease in the system's ability to transfer energy outside of the nominal design point. The use of DSC, on the other hand, enables a wide range of adjustments of the output while realizing MEPT [30].

Robust performance includes the dynamic response and stability of the system, which responds to the ability of the MCWPT to maintain a constant output or optimal efficiency under perturbations. In order to achieve strong robustness, some studies have focused on topology analysis and design [31]. However, the control design of the system directly affects the robustness of the MCWPT [32]. Constant Power Output (CPO) under variable load and variable coupling conditions was achieved by Ref. [33] using TSC based on the principle of parity-time symmetry presented in Ref. [34], and a strong robust CVO was achieved by using RSC in Ref. [35], but both of them add an additional DC/DC converter. DSC, on the other hand, can simplify the circuit topology while improving the robustness, as seen in Ref. [36], and can further reduce the size and cost.

Categorized by the control object, both TSC and RSC belong to Single-Side Control (SSC), i.e., there is the Single-Side Control Magnetic Coupling Wireless Power Transfer (SSC-MCWPT) and the Dual-Side Control Magnetic Coupling Wireless Power Transfer (DSC–MCWPT). In contrast, DSC constitutes a DAB structure with the transmitter side

by using an AR on the receiver side or adding an additional DC/DC converter to make both sides controllable, and such a control strategy not only achieves multiple control objectives at the same time but also simplifies the resonance topology to further optimize the efficiency and improve the robustness of the system to increase the power density of the whole machine.

The advantage of adding a DC/DC converter to realize DSC is that it has little effect on the power conversion link in the intermediate stage of the system but increases the number of components, which increases the size and weight of the system and introduces additional losses. The DAB structure is relatively simple and only needs to be optimally designed for the desired performance in a mature system, which better reflects the advantages of DSC–MCWPT. Therefore, this paper reviews the DSC–MCWPT system based on a single transmitter-single receiver with DAB structures and does not discuss the research papers containing DC/DC converters and multi-transmitter-multi-receiver structures.

This paper is organized as follows, Section 2 introduces the commonly used power conversion topologies, Section 3 introduces the fundamentals of the DSC–MCWPT system, Sections 4 and 5 categorize the various DSC methods, Section 6 summarizes the control methods presented in the previous two sections, Section 7 presents a discussion on the key issues and development trends of the technology, and finally concludes in Section 8.

2. Power Conversion Topology of DSC–MCWPT Systems Based on DAB Converters

The power conversion topology is responsible for regulating the input and output voltages and currents, which is directly related to the design complexity of the DSC, which in turn affects the application scenarios and device selection of the system. Therefore, a categorized discussion is necessary.

2.1. Transmitter-Side Power Conversion Topology

The DSC–MCWPT determines the operating frequency f_s of the system through the TSC, and when f_s is equal to the intrinsic resonant frequencies f_t and f_r of the transmitter and receiver, respectively, the system is in a resonance matching state; otherwise, it is in a resonance mismatching state, which in turn determines the transmission characteristics of the whole system. However, wireless communication is generally required to realize MEPT and the constant output at the transmitter side.

A high-frequency bridge inverter on the transmitter side transforms the DC voltage into a square-wave voltage for injection into the resonance network, which provides flexible voltage regulation and reduces the harmonic content of the output current. In contrast, some studies have used single-switching tube converters such as Class E inverters for implementing bidirectional wireless power transfer [37,38], and although the systems have a smaller size and cost and do not have the possible pass-through problem of bridge inverters, they are, however, difficult to optimize efficiency with DSC.

As shown in Figure 1a,b, half-bridge inverters require only two power switches, so the circuit structure is relatively simple and the driving circuits for the switches are easy to design, making it easy to realize soft-switching. However, the voltage stress on each switch is twice that of a full-bridge inverter, and the amplitude of the transformed voltage is smaller, making it more suitable for low-to-medium power applications. Full-bridge inverters are the most common, and although the number of switches is twice that of a half-bridge, the output capacity is also doubled, making them suitable for high-power applications. However, it is relatively difficult to realize the soft-switching of all switches and requires the design of complex driving circuits.

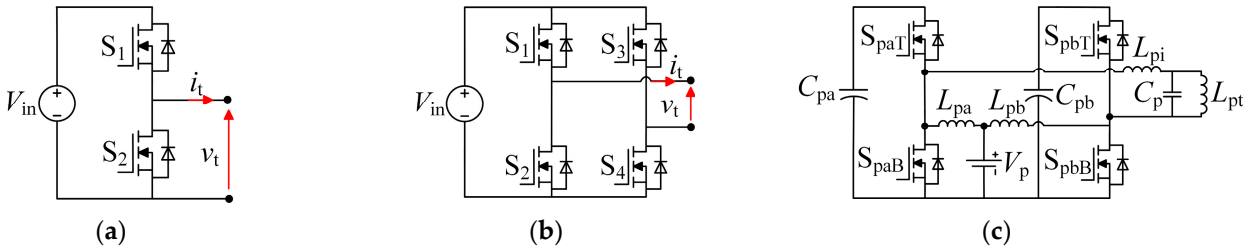


Figure 1. Bridge inverters: (**a**) half-bridge inverter; (**b**) full-bridge inverter; (**c**) boost active bridge inverter [39].

In addition, the interleaved parallel boost inverter combines the boost capability of a boost converter and the high efficiency of a bridge inverter, which can effectively reduce the switching stress. Ref. [39] constructed boost active bridge converters, shown in Figure 1c, which reduce the current stress and switching losses of power switches and have a lower input current ripple compared to the full-bridge inverter.

2.2. Receiver-Side Power Conversion Topology

DSC uses an AR on the receiver side to work with the transmitter side to realize RSC, which is responsible for rectifying and regulating the received high-frequency AC energy to meet the demand of the load and can effectively prevent overvoltage and overcurrent of the output.

When the diode is used as a rectifier, its forward voltage drop is about 0.4~0.7 V, which leads to a large on-state loss in the high-current state; therefore, even if an additional DC/DC converter is added to realize the RSC, its efficiency improvement is limited, especially in low-voltage output applications. In contrast, active bridge rectifiers replace the diode with a power switching device with low on-resistance, which can optimize the rectification efficiency by controlling the on-time sequence. Ref. [40] uses the active half-bridge rectifier of Figure 2a, where only one power switch conducts any switching cycle, eliminating the need for complex isolated drive control, and although switching losses are low, the high voltage stress on the switches is not suitable for high-power applications. In contrast, the active full-bridge rectifier is the most common. As shown in Figure 2b, four switching tubes can be synchronized rectification, can reduce the harmonic content to improve power quality, and are suitable for high-power applications, but this should be at the right time to turn the switch on to reduce hard-switching losses.

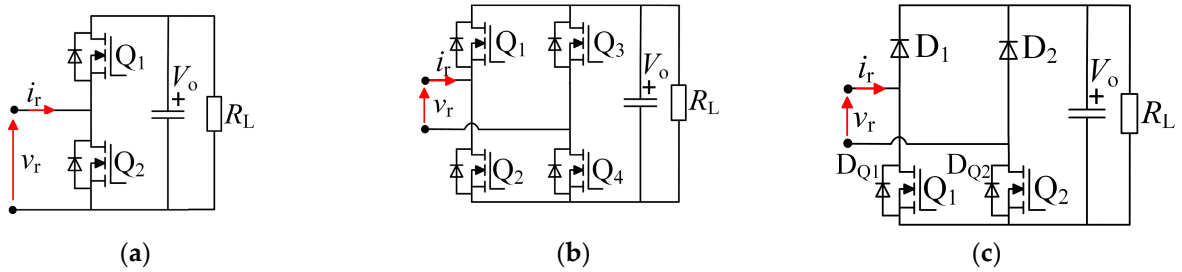


Figure 2. Active bridge rectifiers: (**a**) half-bridge rectifier; (**b**) full-bridge rectifier; (**c**) semi-bridgeless Active Rectifier.

The Semi-Bridgeless Active Rectifier (SBAR) applied in Power Factor Correction (PFC) can also be used on the receiver side of DSC, as shown in Figure 2c, which uses fewer power switches compared to the full-bridge and has a simple driving circuit design, but the diodes exist with a reverse recovery current to bring about losses.

2.3. Comparison of Power Conversion Topologies

In order to compare more intuitively the power conversion topologies used in the DSC methodology presented below, the various combinations of transmitter-side and receiver-side topologies, their types, number of power switches, and their advantages and disadvantages are listed in Table 1.

Table 1. Comparison of power conversion topology combinations.

Type	Transmitter Side	Receiver Side	Number of Power Switches	Advantages	Disadvantages
I	Full-bridge	Full-bridge	8	High transfer power level, high adjustability	High cost, high soft-switching problems
II	Full-bridge	SBAR	6	Moderate control difficulty and cost	High reverse recovery problem of diodes
III	Half-bridge	Half-bridge	4	Low cost, simple structure	Low transfer power level, low adjustability

We can find that there are three main types of power conversion topology combinations for DSC–MCWPT systems based on DAB converters. Type I using a dual-side full-bridge converter has higher tunability due to the largest number of controllable switches, but correspondingly increases the cost and brings soft-switching problems. The SBAR has moderate control difficulty and cost, and the most common application in DSC is to combine it with a full-bridge inverter to form type II, but it is necessary to consider how to inhibit the effect caused by the reverse recovery current of the diode of SBAR. Although the combination of dual-side half-bridge converters of type III requires the least number of power switches, the adjustability is lower.

3. Basic Principles of DSC–MCWPT Systems Based on DAB Converters

As shown in Figure 3, when the system operates normally, the AC power output from the AC grid is usually rectified by the PFC stage and then filtered to provide the inverter with a DC input voltage V_{in}. In most of the papers, the system is analyzed by ignoring the previous rectification and filtering stages, and the DC input is used for the analysis and experiments, so the inputs of the circuits in the following review are all DC sources. Subsequently, the high-frequency inverter converts the DC power into high-frequency AC power. Through the resonance effect of the transmitting coil and compensation network, energy is coupled to the receiver side. Finally, the high-frequency rectification stage converts the high-frequency AC power into DC power for supply to the load.

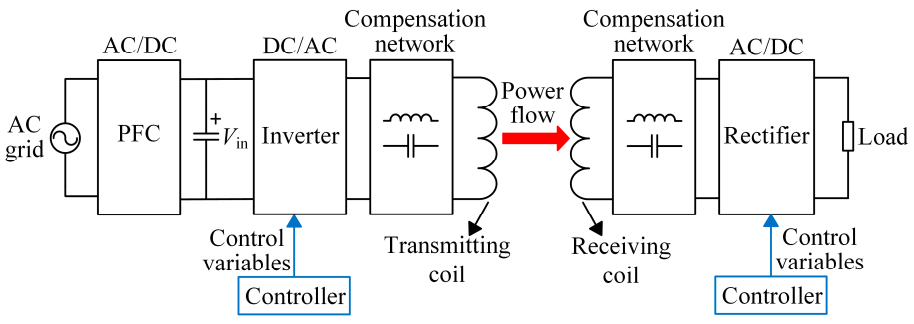


Figure 3. Basic structure of DSC–MCWPT system based on DAB converters.

The value of the compensation capacitance and the intrinsic resonant frequency of the SS topology are independent of mutual inductance and load [41], and its combination with a full-bridge DAB structure is the most commonly used. In order to simplify the analysis process, the following analysis is based on Figure 4a and utilizes the Fundamental Harmonic Approximation (FHA) circuit seen in Figure 4b, where v_t and v_r are the resonant voltages,

and i_t and i_r are the resonant currents. Parameters U_t, U_r, I_t, and I_r are their fundamental components, respectively. Parameters L_t, C_t and L_r, C_r are the resonant inductance and resonant capacitance on the transmitter and receiver sides, respectively. Parameter M is a mutual inductance between inductance coils. Parameter Z_e is the equivalent impedance containing the converter and the DC load, which usually contains the equivalent resistance R_e and the equivalent reactance X_e. Parameters R_t and R_r are internal resistances on both sides.

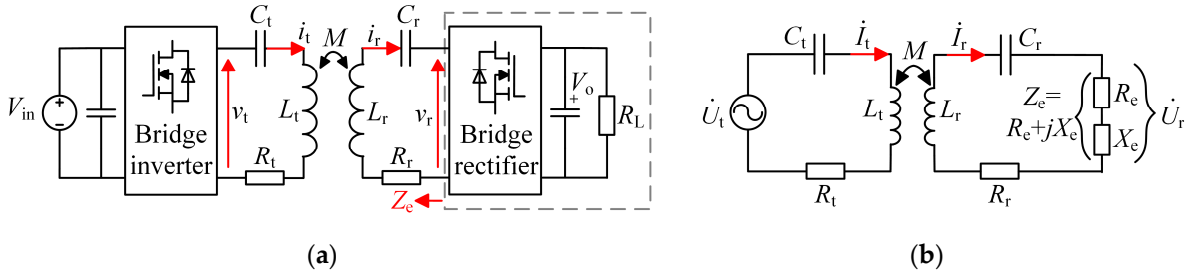


Figure 4. Circuit under analysis: (**a**) DSC–MCWPT system with SS resonant topology; (**b**) FHA equivalent circuit.

The bridge converters mostly adopt pulse width modulation (PWM) Phase Shift Control (PSC), and the control variables are the phase shift angle φ_t on the transmitter side and the phase shift angle φ_r on the receiver side. The switching timing when both sides are subjected to PSC is shown in Figure 5a,b, where $0 \le D_t = \varphi_t/\pi \le 1$ and $0 \le D_r = \varphi_r/\pi \le 1$ are the phase shift duty cycles for the transmitter and the receiver, respectively. Parameters θ_t and θ_r are the voltage–current phase angles, also called the power angles. Parameter δ is the phase angle between the AC-side voltages of the two converters on both sides, also called the external phase shift angle. S_n stands for the transmitter-side power switches, and Q_n stands for the receiver-side power switches, where n is from 1 to 4.

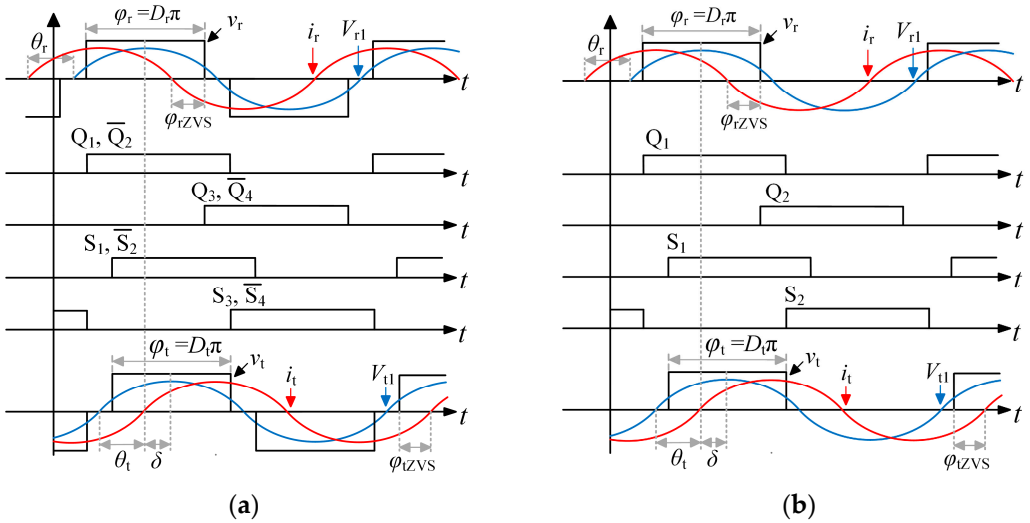


Figure 5. Switching timing waveforms of the dual-side converters: (**a**) full-bridge inverter and rectifier; (**b**) half-bridge inverter and rectifier.

When the full-bridge inverter is subjected to PSC since the switching pulse signals of S_1 and S_2 are complementary and S_3 and S_4 are complementary, the PSC with angle φ_t is realized by fixing the duty cycle of each switch to 0.5 and letting S_4 delay φ_t turn on with respect to S_1, i.e., delaying the φ_t turn on of S_2 with respect to S_3, and the same is true for the PSC of the active full-bridge rectifier. The φ_t and φ_r of the half-bridge converter are complementary and cannot realize PSC and the output voltage can only be adjusted by

adjusting the duty cycles D_t and D_r, and there are only two states, V_{in}, 0 or V_o, 0, in a cycle, so it has a relatively low voltage regulation capability.

The SBAR can implement synchronous rectification [42] or soft-switching [29], but its PSC operates differently from the full bridge, not by phase shifting through the overlap of the two drive pulses but by controlling the magnitude of the phase θ_c between the point where the resonant current passes through zero and the drive pulse. As shown in Figure 6a,b, from the moment of t_1, Q_2 is driven to conduct, the current flows forward in the resonant circuit, and the current flows in reverse at the moment of t_2. If Q_1 conducts at this time, it is impossible to realize soft-switching, and therefore, in the time of t_2–t_3, the body diode of Q_1 is first allowed to conduct, and after the voltage of Q_1 is clamped to zero, Q_1 is made to drive to conduct at the moment of t_3 to realize the ZVS; at this time, parameter θ_c is equal to $(1 - D_r)\pi$.

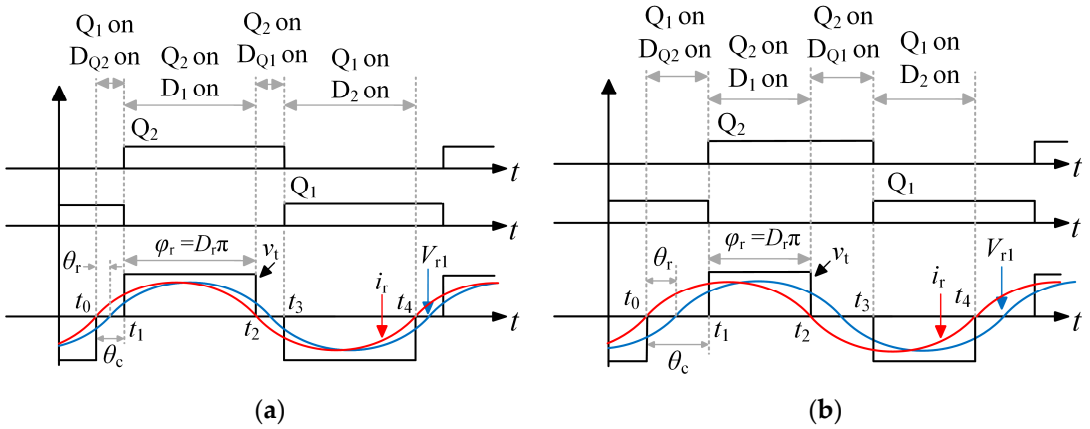


Figure 6. Waveforms of the SBAR under PSC: (**a**) D_r is larger; (**b**) D_r is smaller.

Whether it is a full-bridge converter, half-bridge converter, or a SBAR, its AC-side voltage and DC-side voltage under FHA satisfy the following equation:

$$\begin{cases} \dot{U}_t = K_t V_{in} \sin(\varphi_t/2)\angle 0 \\ \dot{U}_r = K_r V_o \sin(\varphi_r/2)\angle \delta, \end{cases} \tag{1}$$

where K_t and K_r are the DC/AC voltage conversion ratios. For a full-bridge converter, K_t and K_r are equal to $2\sqrt{2}/\pi$. For a half-bridge converter, K_t and K_r are equal to $\sqrt{2}/\pi$ For a SBAR, K_r is equal to $2\sqrt{2}/\pi$.

According to the Kirchhoff voltage equation, by writing equations for both sides separately, we can obtain:

$$\begin{cases} \dot{U}_t = \dot{I}_t(R_t + j\omega X_t) - j\omega M\dot{I}_r \\ j\omega M\dot{I}_t = \dot{I}_r(R_r + j\omega X_r + R_e + j\omega X_e), \end{cases} \tag{2}$$

among them:

$$\begin{cases} X_t = j\omega L_t - j\frac{1}{\omega C_t} \\ X_r = j\omega L_r - j\frac{1}{\omega C_r}. \end{cases} \tag{3}$$

According to Equation (1) and Figure 4b, the input power and output power of the system can be obtained, and further, the transmission efficiency of the system can be obtained, as seen in Ref. [43]:

$$\eta = \frac{\omega^2 M^2 R_L}{\omega^2 M^2 (R_e + R_r) + R_t[(R_e + R_r)^2 + (X_e + X_r)^2]}. \tag{4}$$

In order to achieve optimal efficiency under different loads, it is necessary to implement IM, which is derived from the general expression of Equation (4) for the system efficiency when the total reactance on the receiver side is $X_{rt} = X_r + X_e = 0$; let $d\eta/dR_e = 0$, at which point there exists an optimal equivalent load resistance R_{eopt}:

$$R_{eopt} = R_r\sqrt{1 + \frac{\omega^2 M^2}{R_t R_r}}. \tag{5}$$

At this time, the influence of internal resistance cannot be ignored, and each M corresponds to a specific excitation voltage ratio: $T_{ac} = U_r/U_t$. Neglecting the rectifier losses, the equivalent resistance R_e and equivalent reactance X_e can be obtained from Equation (6) according to the law of energy conservation: $U_r I_r = V_o I_o$. Therefore, the DSC can realize the IM by adjusting the phase shift duty cycle D_r and power angle θ_r of the receiver to change R_e and X_e.

$$\begin{cases} R_e = K_r^2 R_L \sin^2(\frac{D_r\pi}{2})\cos^2\theta_r \\ X_e = K_r^2 R_L \sin^2(\frac{D_r\pi}{2})\sin\theta_r\cos\theta_r \end{cases} \tag{6}$$

When the resonance matching states U_t, U_r, I_t, and I_r can be regarded as sinusoidal waveforms, and the relationship between the fundamental waveform components is expressed as the following equation, at this time, the internal resistances of the inductor coil, R_t and R_r, can be ignored.

$$\begin{cases} \dot{I}_t = \frac{\dot{U}_r}{j\omega M} \\ \dot{I}_r = -\frac{\dot{U}_t}{j\omega M} \end{cases} \tag{7}$$

According to the above equation, the phasor diagram is shown in Figure 7, where there is a phase relationship:

$$\theta_t = \theta_r = \frac{\pi}{2} - \delta. \tag{8}$$

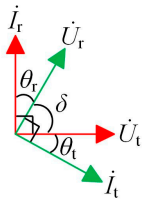


Figure 7. Phasor diagram of SS topology resonance matching.

To enhance transmission efficiency and minimize Electromagnetic Interference (EMI) in the system, it is necessary to implement a Zero-Voltage Switching (ZVS) operation on commonly used semiconductor devices. For this reason, the ZVS angle in Figure 5 is shown in Equation (9), and φ_{tZVS} and φ_{rZVS} must be greater than or equal to zero in order for the parasitic diode to conduct first and realize zero-voltage turn on when the MOSFET tube is driven on.

$$\begin{cases} \varphi_{tZVS} = \theta_t - (1 - D_t)\frac{\pi}{2} \\ \varphi_{rZVS} = \theta_r - (1 - D_r)\frac{\pi}{2} \end{cases} \tag{9}$$

Combined with Equations (8) and (9), the conditions for realizing ZVS can be expressed as:

$$\begin{cases} \delta \le \frac{\varphi_t}{2} \\ \delta \le \frac{\varphi_r}{2}. \end{cases} \tag{10}$$

According to Equations (1) and (7), the active and reactive components of the output power at the bridge rectifier side can be expressed as:

$$\begin{cases} P = K_t V_o \sin(\frac{\varphi_r}{2}) \cos\theta_r = \frac{K_t K_r V_{in} V_o}{\omega M} \sin(\frac{\varphi_t}{2}) \sin(\frac{\varphi_r}{2}) \sin\delta \\ Q = K_r V_o \sin(\frac{\varphi_r}{2}) \sin\theta_r = \frac{K_t K_r V_{in} V_o}{\omega M} \sin(\frac{\varphi_t}{2}) \sin(\frac{\varphi_r}{2}) \cos\delta. \end{cases} \tag{11}$$

It can be seen that the reactive power Q is proportional to δ. The DSC strategy can widen the ZVS range of the power switches on both sides under different operating conditions by controlling δ. Eventually, the power angles θ_t and θ_r on both sides will increase, which inevitably leads to an increase in the reactive power loss of the system, so the ZVS angle should be close to zero. To further optimize the efficiency, the external phase shift angle should be satisfied:

$$\delta = \min(\frac{\varphi_t}{2}, \frac{\varphi_r}{2}). \tag{12}$$

At this time, the efficiency of the system can be expressed as:

$$\eta = \frac{P}{P + P_{loss}} = \frac{{I_r}^2 R_e}{{I_r}^2 R_e + {I_r}^2 R_r + {I_t}^2 R_t} = \frac{\omega M \sin\delta}{R_r / T_{ac} + T_{ac} R_t + \omega M \sin\delta}, \tag{13}$$

where P_{loss} denotes the active power loss and T_{ac} can be expressed as:

$$T_{ac} = \frac{U_r}{U_t} = \frac{K_r V_o \sin(\varphi_r/2)}{K_t V_{in} \sin(\varphi_t/2)}. \tag{14}$$

According to the above equation, the efficiency optimization method of Load Matching (LM) has been mentioned in many DSC articles, where the best efficiency for a certain optimal excitation voltage ratio T_{acopt} can be obtained by making $d\eta/dT_{ac} = 0$. Since DSC–MCWPT systems often use symmetric parametric designs with equal internal resistance on both sides, the condition for realizing LM in the structure of Figure 4a is shown in Equation (15) [44]:

$$T_{acopt} = \frac{U_r}{U_t} = \sqrt{\frac{R_r}{R_t}} = 1. \tag{15}$$

Usually, internal resistances R_t and R_r are very small, and variable $\omega^2 M^2/(R_t R_r)$ is much larger than 1, so R_{eopt} and T_{ac} can be simplified as follows:

$$\begin{cases} R_{eopt} \approx \omega M \sqrt{\frac{R_r}{R_t}} \\ T_{ac} = \frac{\omega M}{R_t R_r + R_t R_e + \omega^2 M^2} R_{eopt} \approx \sqrt{\frac{R_r}{R_t}}. \end{cases} \tag{16}$$

Thus, LM and IM are the same—just another form of control expression. In addition, combining Equations (7), (14), and (15), and defining the ratio of the magnitude of the resonant currents on both sides as $T_i = I_t/I_r$, the T_{iopt} at this point for realizing LM under the T_{acopt} can be expressed, as seen Equation (17). Therefore, controlling both sides of the resonant current RMS values to be equal is also equivalent to realizing LM. The significance of adjusting T_{ac} in a way to optimize the efficiency can be explained as follows: according to the different circuit parameters of the system, adjusting the phase angle to change T_{ac} leads to changes in the magnitude of the resonant currents on both sides, which results in a more even distribution of the conduction losses and improves the efficiency as much as possible for different operating conditions. The MEPT methods by which variables R_e, T_{ac}, or T_i are adjusted are collectively referred to as IM in the following equation.

$$T_{iopt} = \frac{I_t}{I_r} = \sqrt{\frac{R_r}{R_t}} = 1 \tag{17}$$

From the above analysis, it is concluded that the transmission characteristics of the MCWPT systems are affected by the relative position between the coils, load, resonant frequency, and parasitic parameters. However, the synchronization of the control signals of the transmitter and receiver sides under DSC is also crucial. If the phase of δ is kept constant under a certain operating point, i.e., the AC voltages on both sides are kept in a constant phase to achieve phase synchronization, the stability of the control loop can be ensured. However, the method of phase synchronization of the control signals depends on whether wireless communication is added or not.

4. Control Strategies with Wireless Communication for DSC–MCWPT Systems Based on DAB Converters

With wireless communication, the information on this side is directly sent to the other side through a Radio Frequency (RF) module, which is relatively simple in achieving a constant output, efficiency optimization, or soft-switching, but the stability and reliability of communication need to be fully considered.

4.1. Dual-Phase Shift Control Strategy

The DAB converter-based DSC–MCWPT using Dual-Phase Shift Control (DPSC) with communication can realize MEPT, and the control variables are phase shift angles φ_t and φ_r. Generally, the receiver side adjusts the load to optimize the efficiency, and the transmitter side can obtain the information of the other side based on the wireless communication feedback to achieve a constant output.

Li et al. [45] proposed a current–stress optimization strategy based on DPSC. In order to realize CVO, the use of TSC must make I_t constant, which leads to a large difference in the resonant current values on both sides and thus to higher losses. From the theoretical analysis in the previous section, only when I_t is equal to I_r does the resonant current cause less loss, which is equivalent to being able to realize IM. Adjusting the phase shift angle on both sides can change the size of the resonant current on both sides and δ fixed at 90° can minimize the Q of the system at the resonant frequency. Therefore, the control strategy is shown in Figure 8. The PI control is performed on the receiver side to regulate the φ_r to maintain CVO or CCO, where V_{oref} and I_{oref} are given as reference values. Parameters V_o and φ_r are sent to the transmitter-side controller, which first calculates the DC voltage ratio T_{dc} and then obtains φ_t based on the calculation results of the current stress optimization, and then φ_t and φ_r can be synchronously varied to achieve the equalization of current stress. The maximum current stress is reduced, although the current magnitude may be elevated on both sides. This control strategy enables the MEPT process to counteract the variation of coupling coefficients and loads without mutual inductance estimation and therefore has good robustness.

Zero Phase Angle (ZPA) control removes reactive power from the resonant topology and is a simple way to implement IM. In general, regarding the flow of the ZPA, as shown in Figure 9, the current i_t is converted by the current sampling circuit into a voltage signal u_c, which is sent to the Zero-Crossing Detection (ZCD) circuit to generate a square wave signal S_t with the same frequency and phase as i_t, which is then sent to the DSP as a synchronization signal to generate PWM signals, ultimately driving the circuit controls and the power switch and outputting a square wave voltage u_t in phase with i_t. However, the current transformer and low-pass filter used in the current sampling circuit are susceptible to high-frequency EMI, which results in the loss of the synchronization signal generated by the zero-crossing point, resulting in the erroneous conduction of the switch and affecting the safe operation of the system.

Therefore, Jiang et al. [46] used a Phase-Locked Loop-Chain Triggered Mode (PLL-CTM) to accurately lock the phase of the resonant currents to reliably generate drive pulses for IM and CCO/CVO charging under DPSC. CTM refers to letting the counter of PWMx be used sequentially as a trigger signal to generate the counter of PWMx + 1, similar to the PWM control of the STM32 controller in master–slave operation mode, which can

effectively avoid the problem of losing synchronization pulses. The Phase-Locked Loop (PLL) in the article is based on a double D flip-flop circuit and DSP's Cap module for phase detection, combined with the PI algorithm for phase locking as shown in Figure 10a,b. The hysteresis comparator generates the voltage signal i_{r1} with hysteresis φ_s, and the rising edge generates the synchronization signal S_{n1}, which is used to load the counting value of the counter CNT1 of the PWM1, and once the CNT1 counts to zero, it generates the synchronization signal S_{n2} and the reference signal S_{1A}, which are used to load the counting value of the PWM2, and so on. Therefore, the key to the success of the PLL lies in the generation of S_{1A}. S_{ph} is measured by the Cap module for determining the phase difference between S_{n1} and S_{n2}, and φ_{ifb} is calculated and adjusted with the reference value φ_{iref} by the PI algorithm to precisely control the phase of the reference signal. However, the effect of the coupling coefficient is not considered, and the transmitter side requires wireless communication for CCO/CVO adjustment, which reduces the dynamic performance to some extent.

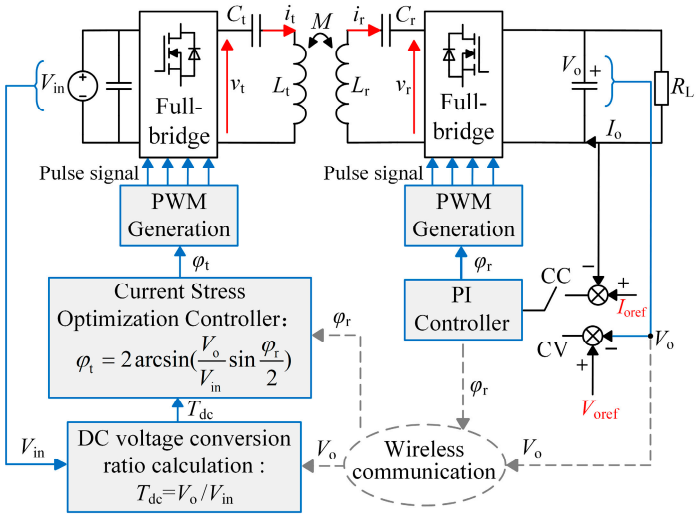


Figure 8. Diagram of the proposed current stress optimization control strategy [45].

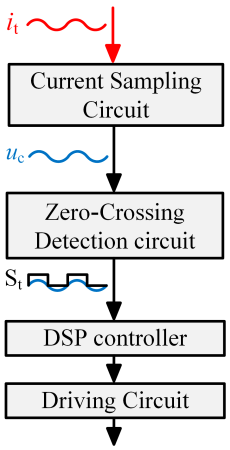


Figure 9. Flowchart of ZPA control.

Wang et al. [47] used DPSC to realize IM over a wide output power range. The output voltage V_o and output current I_o are sampled at the load side, and the output current is kept constant by controlling the phase shift angle φ_r through PI. The transmitter side learns V_o through wireless communication and measures the mutual inductance through estimation, and finally, it controls the phase shift angle φ_t to realize the power output under IM. In order to eliminate the reactive component and ensure that the outward phase shift angle δ is constant at 90°, a method of tracking the maximum I_o peak is proposed to achieve this.

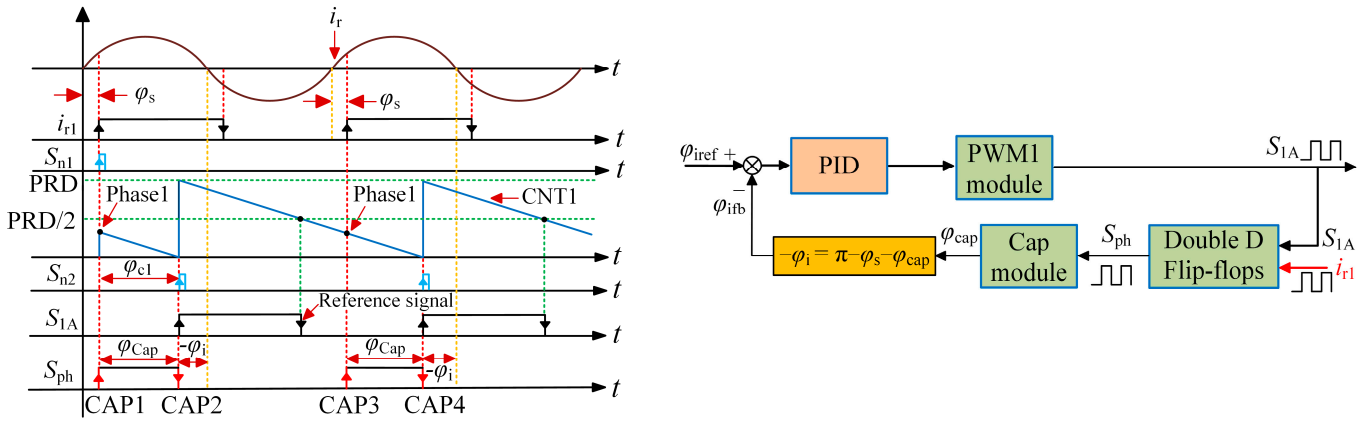


Figure 10. Proposed PLL control strategy [46]: (**a**) operating waveforms of the proposed PLL; (**b**) control diagram of the proposed PLL.

In order to improve the dynamic process of DPSC, Ref. [48] analyzes the phase shift angles φ_{topt} and φ_{ropt} at optimal efficiency for each output power. However, when the output power varies, the usual DPSC methods make a step change $\Delta\varphi$ in φ_t and φ_r, which inevitably causes overcurrent problems. Therefore, the control method divides the phase shift angle change in the dynamic process into multiple steps and keeps the current change increment under each step below 1.1 times. However, the method makes the dynamic time longer, as shown in Figure 11.

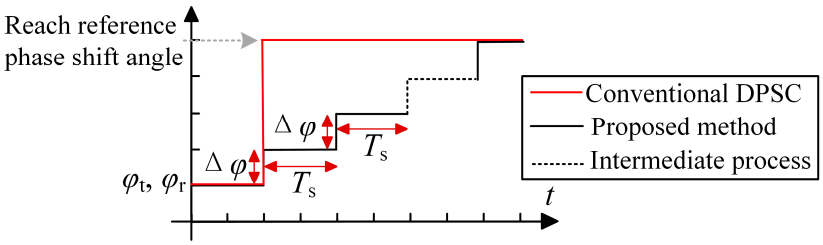


Figure 11. Comparison of the regulation process under the conventional and the proposed DPSC control [48].

4.2. Triple Phase Shift Control Strategy

DPSC usually keeps δ fixed at 90°, and MEPT under variable load and variable coupling can be realized by adjusting φ_t and φ_r. However, it is difficult to realize ZVS for all switches with conventional DPSC methods. In order to reduce the switching losses, Three Phase Shift Control (TPSC) can further optimize the system efficiency by controlling the external phase shift angle δ of the converter or the power angle θr of the AR, which can broaden the ZVS ranges of the switches on both sides under different output conditions.

Typical TPSC methods easily realize the ZVS of power switching and bidirectional flow of power by introducing δ. From Equation (11), the active power flows from the transmitter side to the receiver side when $0 < \delta < \pi$, and the power flow is reversed when $-\pi < \delta < 0$. The power flow is minimized in both directions by the ZVS and further efficiency optimization. In Ref. [49], δ was controlled to $\pm 90°$ to minimize the reactive power while achieving a bidirectional transmission of power, but ZVS and further efficiency optimization were not achieved.

Zhang et al. [50] realized IM with soft-switching by using δ as an additional control variable. First, since FHA will have a large error in analyzing the ZVS condition, the article analyzes it through a time domain model, which takes into account the effect of the parasitic capacitance C_{oss} at the two ends of the power switches and derives the equations of the

time domain condition for realizing the ZVS conduction of all the switches. According to the analysis in Section 3, δ can only be deviated from $\pm 90^\circ$ to make the voltage and current show a certain degree of inductance, realizing ZVS, but inevitably bringing additional reactive power loss. Therefore, $\Delta\delta$ is used to denote the degree of divergence from $\pm 90^\circ$, allowing the system to satisfy ZVS and IM over the operating range while reducing $\Delta\delta$. This approach also considers effectiveness at different coupling coefficients but does not further optimize the system's efficiency at different output voltages and lacks a complete control loop design.

Therefore, Ref. [44] examined the IM conditions for different DC voltage gains $T_{dc} = V_o/V_{in}$ in order to optimize the efficiency of the TPSC over a wide voltage output range, called segmented TPSC. The control flowchart is shown in Figure 12a, and the overall closed-loop controller is shown in Figure 12b, where only PI is used on the transmitter side to realize the CVO, and the main control algorithm is placed on the receiver side, so wireless communication is needed to pass the information.

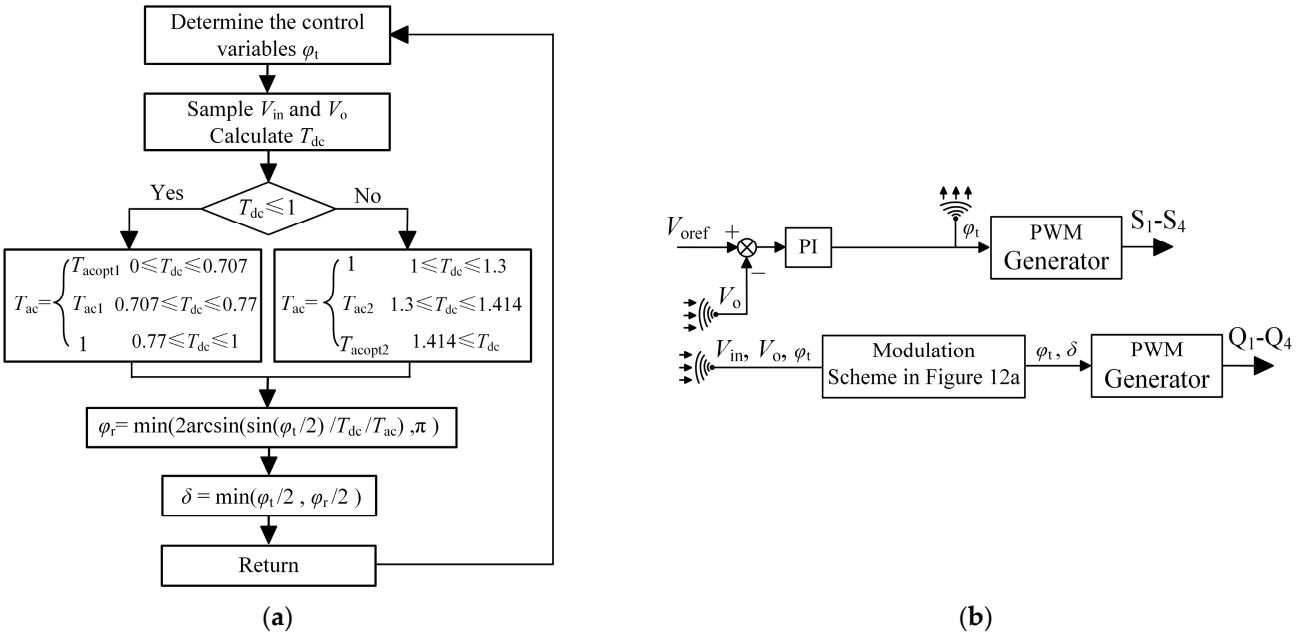


Figure 12. Proposed segment TPSC strategy [44]: (**a**) flowchart; (**b**) closed-loop control diagram.

The authors point out that if δ and T_{dc} are varied, the conditions for realizing IM change, and that to optimize the efficiency, it is necessary to segment the modulation at boost ($T_{dc} > 1$) and buck ($0 < T_{dc} < 1$) voltages. First, consider optimizing the losses due to the current stress imbalance on both sides by making $\varphi_t \leq \varphi_r$ when operating in buck mode and letting $\varphi_t \geq \varphi_r$ when operating in boost mode. Then, according to Equations (12) and (13), the optimal excitation voltage ratio T_{acopt} in the two operating modes can be derived. The conclusion is thus: when $T_{dc} \geq \sqrt{2}$, let $\varphi_t \geq \varphi_r$, at which time $T_{acopt} = \sqrt{2}/2$. When $T_{dc} \leq \sqrt{2}/2$, let $\varphi_t \leq \varphi_r$, at which time $T_{acopt} = \sqrt{2}$. However, when $\sqrt{2}/2 \leq T_{dc} \leq \sqrt{2}$, the system fails to achieve the T_{acopt} and may fail to operate stably if it operates at the boundary of mode switching. Therefore, the transmission efficiencies on both sides of the boundary are obtained separately, and the T_{dc} that enables the system to maintain the same efficiency in the transition mode is obtained, which ensures that T_{ac} can be linearly transformed during the transition process.

In order to design faster wireless chargers, Ref. [51] implements a CPO scheme and efficiency optimization strategy using TPSC. The transmitter-side controller achieves ZVS and minimizes the reactive power loss by regulating the φ_t and δ. Therefore, wireless communication is required to synchronize the phase of the AC voltages on both sides. The receiver side regulates the output power by controlling φ_r, and the efficiency optimization

is achieved by adjusting φ_t, φ_r, and δ to keep the resonant current stresses on both sides in balance.

By controlling δ, it is necessary to synchronize the phase of the drive signals on both sides with the help of wireless communication, which makes it difficult to achieve precise adjustment, and it is easier to realize TPSC by adjusting the power angle of AR when the three phase control degrees of freedom are φ_t, φ_r, and θ_r.

Ref. [52] proposed the joint control with variable ZVS angles in order to realize the ZVS and the desired output voltage for all switches. The authors found that there is only a certain region where the ZVS of the dual-side converters can be realized simultaneously, and in order to optimize the efficiency, both the resonant network and the converter losses are taken into account to derive the conditions to achieve the minimum power loss at the boundary of this region, i.e., the combinations of φ_t, φ_r, and θ_r for different powers. The transmitter side samples V_{in} and I_{in} and sends them to the receiver side through wireless communication, and the receiver side samples V_o and I_o, which are used to calculate the efficiency and T_{dc} and regulate the CCO/CVO by using PID. The authors derive in detail the power losses and their boundary conditions under different operating regions, which improve the efficiency under light loads, resulting in a significant reduction of switching and reactive power losses, and which are applicable to different coupling coefficients and loads.

The parameter drift of the resonant element causes the resonant reactance $X_r \neq 0$, $X_{rt} \neq 0$, which leads to the system detuning. The conventional IM method does not consider the compensation of X_e in case of detuning. Therefore, Ref. [53] adds an Auxiliary Measurement Coil (AMC) at the receiver side based on the TPSC to form an Active Single-Phase Rectifier (ASPR). The authors point out that allowing the resonant current i_r to exceed u_r in order to turn on the MOSFET for ZVS leads to an increase in the equivalent reactance X_e, which increases θ_r, which in turn leads to a decrease in the maximum adjustable range of equivalent resistance R_e, resulting in difficulty in achieving IM at light loads. In order to decouple the two control variables, θ_r and φ_r, with respect to R_e and X_e, an auxiliary control is performed using an AMC, as shown in Figure 13. The primary turns of the decoupling transformer are only 1 or 2, and L_{tr} is compensated by C_r, so it has little effect on the resonant conditions. When M_T is equal to M_{RM}, the open-circuit voltage V_{meas} of the AMC is in phase with U_r, so the angle θ_{AMC} between V_{meas} and i_r can be measured for regulating R_e and X_e. Firstly, parameter R_{eopt} is calculated and V_o is transmitted to the transmitter-side controller via wireless communication, and a PI controller is used to adjust φ_t to achieve CVO, parameter I_o and V_o, which are sampled for measuring R_L. Variable θ_{AMC} is used to determine X_e and R_e, when $X_e = -R_e \times \arctan(\theta_{AMC})$ represents fully compensated reactance X_r. This method widens the range of IM but does not fully realize the soft-switching.

4.3. Variable Frequency Multi-Phase Shift Control Strategy

It is difficult to realize multiple control objectives when system parameters such as mutual inductance are varied. Therefore, some research has proposed Variable-Frequency Three Phase Shift Control (VFTPSC) to realize ZVS operation under wide load variations by using a multivariable control with φ_t, φ_r, δ, f_s or φ_t, φ_r, θ_r, and f_s, which is also known as a hybrid or multivariable control.

Liu et al. [54] utilized the VFTPSC strategy to reduce the system efficiency degradation due to coil misalignment. The system control block diagram is shown in Figure 14. The receiver side adjusts the output power P_o by controlling φ_r, and achieves ZVS on both sides by controlling θ_r. Meanwhile, variables φ_r and θ_r work together to change equivalent resistance R_e to achieve IM. The regulation of the operating frequency f_s is used to control the equivalent reactance X_e to compensate for the resonant reactance X_r, keeping the total reactance X_{rt} always at zero. However, there are different f_s at different P_o and M. The transmitter-side control controls the inverter based on the information received from the wireless communication in conjunction with a look-up table built from φ_t, P_o, M, and f_s.

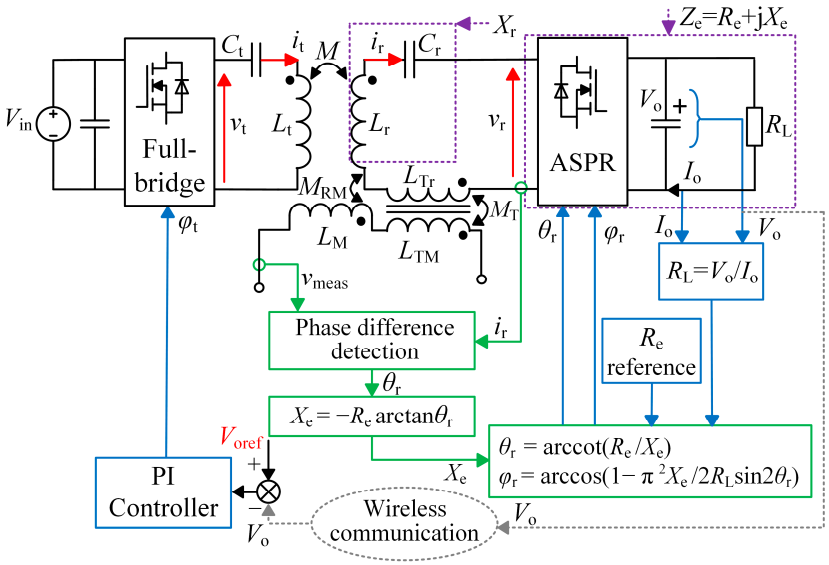


Figure 13. Proposed TPSC method based on AMC [53].

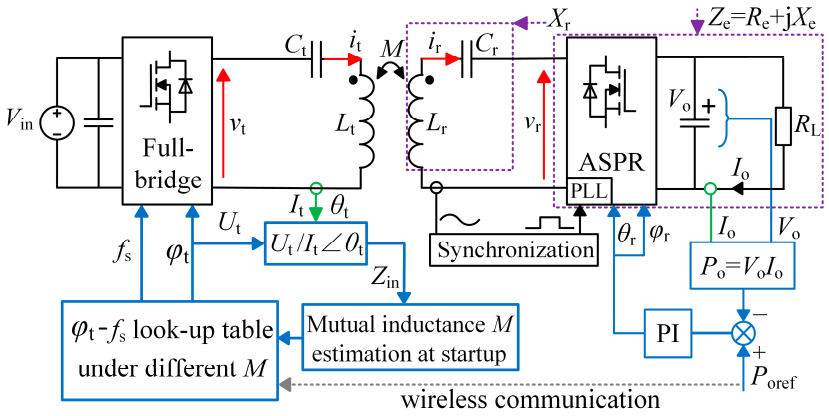


Figure 14. Proposed multivariable control strategy [54].

Ref. [55] achieves the efficiency optimization of a system with high-order compensation topology over a wide output power range by VFTPSC with ZVS conditions obtained using an extended time domain model. First, the phase shift angle φ_r corresponding to the R_{eopt} that satisfies the IM is calculated based on the desired output power P_o and the load R_L. The transmitter side obtains the information of M and P_o through mutual inductance estimation and wireless communication and controls the phase shift angle φ_t to realize the CPO. Then, the authors derive the minimum external phase shift phase angle δ_{ZVS} for the simultaneous realization of ZVS on both sides. Based on φ_r, φ_t, and f_s at this point, the external phase shift angle δ is calculated and adjusted to satisfy the ZVS operation on both sides while limiting the magnitude of δ to reduce the reactive power loss. Finally, the operating frequency is changed so that the total reactance X_{rt} is small enough and the frequency is updated to return to the first step to re-regulate. The control flowchart is shown in Figure 15.

Huang et al. [56], on the other hand, utilized variable frequency control to improve the dynamic performance of the switching process for CCO and CVO charging. The authors analyze the system with a discrete-time model, obtain the relationships of φ_t, φ_r, and δ with fs according to different switching timings, and derive the conditions for all switches to realize ZVS. The controller has two main parts. First, the range recognition module regulates δ to ensure that the system operates in the ZVS region. The optimization and regulation module determines φ_t, φ_r, and f_s by sampling the output voltage and output current, while the parameters of φ_t, φ_r, δ, and f_s to achieve the minimum reactive power

loss in different operating states are solved numerically and made into look-up tables to be stored in the controller at the receiver side; thus, wireless communication is required to pass the information to the transmitter-side controller. In contrast, this method eliminates the need to adjust the switching frequency away from the intrinsic resonant frequency of the system.

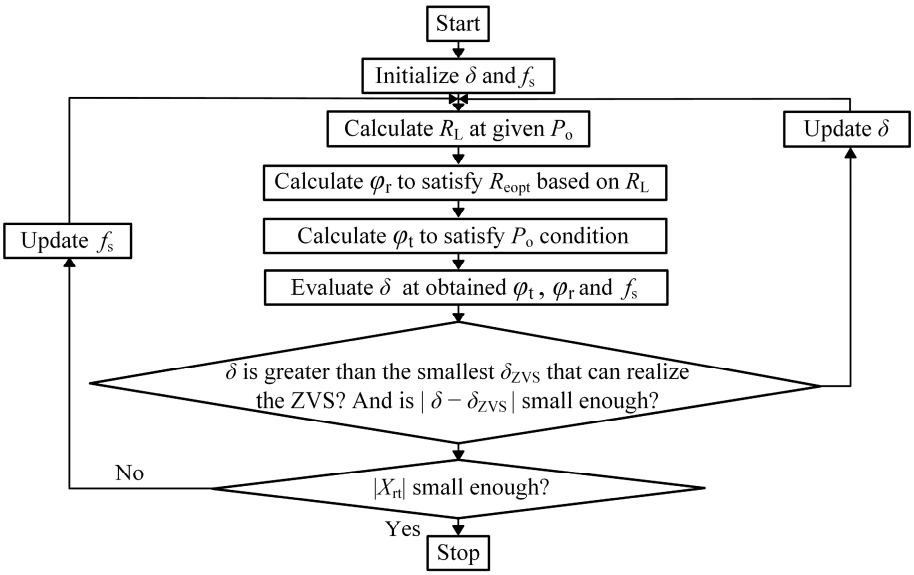


Figure 15. Flowchart for determining optimal values of φ_t, φ_r, δ, and f_s [55].

The capacitive drift of the resonant network causes the system to be detuned and reduces the output power and efficiency. Ref. [57] achieved dual-side tuning using Variable Frequency Control (VFC) and PSC, and the system structure is shown in Figure 16. The transmitter side detects the phases of θ_t and θ_r, adjusts the operating frequency to keep the resonant reactance X_t constant at zero, and adjusts the phase shift angle φ_t to keep the external phase shift angle δ constant at 90°, where the acquisition of θ_r is realized by an auxiliary coil integrated with the transmitting coil. The receiver-side phase shift angle φ_r is constant, the information of X_r is received through wireless communication, and θ_r is adjusted to eliminate the receiver-side total reactance X_{rt}. Compared with the common tuning method, this DSC strategy does not require communication to transmit the phase information and has a faster stabilization time.

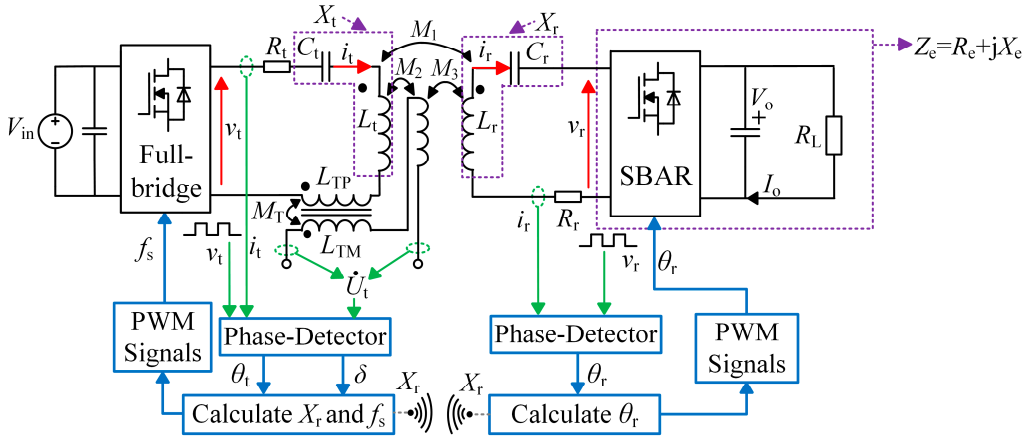


Figure 16. Proposed control diagrams of the tuning method [57].

Ref. [58] proposes a novel current-controlled SBAR to meet the CCO charging of step-up loads such as supercapacitors. The receiver side realizes IM by adjusting the phase

shift angle φ_r through PSC to improve the transmission efficiency, and the transmitter side receives the phase information through wireless communication and realizes the CCO by adjusting the operating frequency and keeping it at a high bifurcation frequency to realize ZVS.

4.4. Mode-Switching Control Strategy

TPSCs relying on external phase shift phase angle δ regulation make it easy to realize ZVS; however, this comes at the cost of lowering the power factor, the wide ZVS range inevitably leads to an increase in reactive power losses at light loads, and the system still struggles to achieve optimal efficiency. The mode-switching control (MSC) strategy effectively increases δ through a combination of switching modes; e.g., by making the full-bridge converter operate in half-bridge mode to reduce the voltage conversion gains K_t and K_r. Depending on the loads, making the output of the converter lower than the rated voltage value can effectively increase δ, which reduces the reactive power generated by the converter and at the same time ensures its ZVS operation to further optimize the efficiency. However, most of this DSC strategy requires wireless communication because the mode controller needs load information from the receiver side.

As shown in Figure 17a, a full-bridge converter is used on both sides, and the full-bridge converter can be made to operate in the half-bridge mode by making S_1 and Q_1 normally on and S_3 and Q_3 normally off in one cycle. The system has four operating modes, namely Full-Bridge–Full-Bridge (FB–FB), Half-Bridge–Full-Bridge (HB–FB), Full-Bridge–Half-Bridge (FB–HB), and Half-Bridge–Half-Bridge (HB–HB). The mode controller determines whether the converter is operating at FB or HB based on the output voltage V_o and output current I_o.

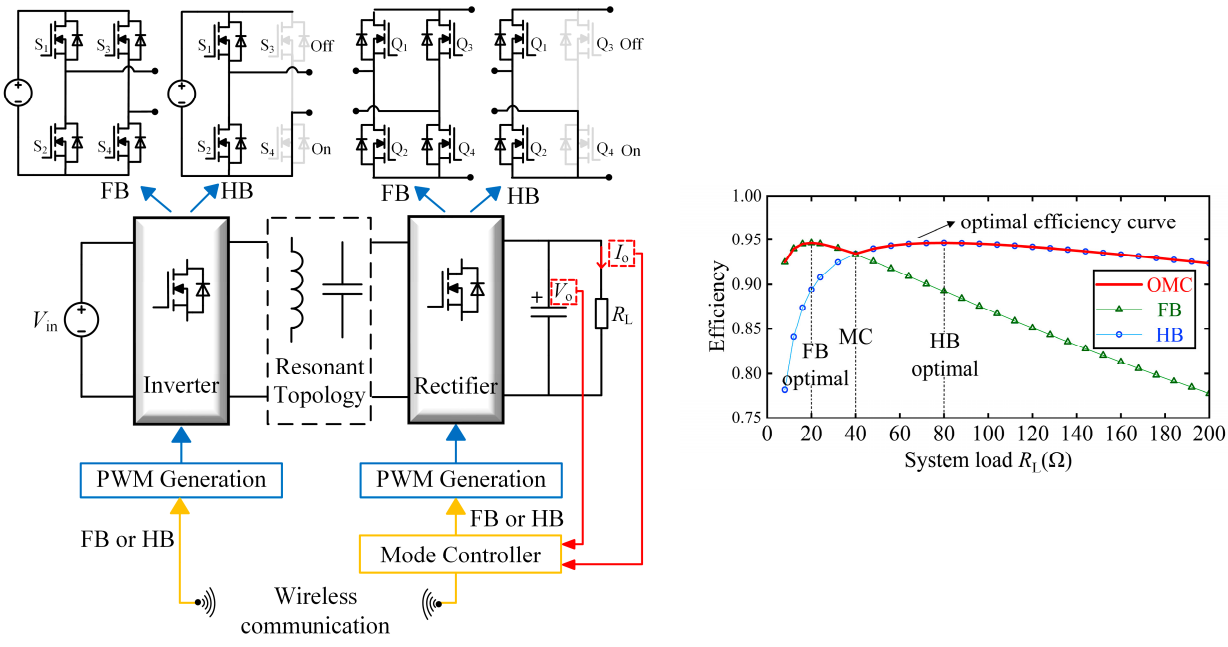


Figure 17. Implementation of a mode-switching control strategy [59]: (**a**) system structure; (**b**) theoretical efficiency under mode switching.

In Ref. [59], a mode-switching strategy was proposed for extending the IM range by allowing the converter to change from FB to HB at the same time at the Mode Changing (MC) point so that the system always tracks the Optimal Efficiency Curve (OMC), as shown in Figure 17b. The system has two modes of operation, FB–FB and HB–HB. The overall control structure of the system is shown in Figure 17a. First, the mode controller calculates the optimal equivalent load R_{eopt}, the receiver side calculates R_L by sampling V_o and I_o,

the mode controller selects the operating mode according to R_L, and the wireless communication module is used to inform the operating state of the transmitter side at the MC point. Although the control strategy is simplified, the ZVS is not realized. Wang et al. [60], on the other hand, implemented ZVS, and the proposed mode-switching strategy switches both sides to half-bridge converter operation below 1/4 of a full load and regulates T_{ac} by DPSC to achieve IM and optimizes reactive power loss under light load ZVS operation.

The MSC strategy proposed in Ref. [61] has a total of three operating modes (FB–FB, HB–FB, and HB–HB), and the operating point can be determined by judging the output power P_o. The receiver side calculates P_o by sampling V_o and I_o, and adjusts φ_r in real time to realize IM, so the transmitter side needs wireless communication to adjust φ_t to realize CVO, and δ follows the change of φ_t and φ_r to realize the ZVS. It can be seen that there are three control degrees of freedom of φ_t, φ_r, and δ on top of MSC, which is equivalent to the combination of MSC and TPSC. However, it enables the system to further improve the efficiency in a wider power range and solves the contradiction of the TPSC to achieve ZVS under light load, resulting in higher resonant current and reactive power. However, the effect of the coupling coefficient on the output and control stability cannot be neglected.

Zhu et al. [62] further improved the control capability of the MSC by proposing a control strategy that enables the system to operate in the mixed-bridge (MB) mode, when the inverter alternately operates in FB and HB, which can effectively expand the regulation range of the converter output voltage. As shown in Figure 18a, the converter operates in FB in one of the two switching cycles and in HB mode in the other, when the rms values U_t and U_r can still be expressed in terms of (1), but in this case, $K_t = K_r = 3\sqrt{2}/2/\pi$. A total of seven operating modes exist in the system and the mode switching is still determined by the output power P_o, and the conditions of IM and ZVS are further considered. The circuit and control structures are shown in Figure 18b. The transmitter side regulates φ_t to realize IM, and the receiver side controls φ_r to realize CVO and ZVS by regulating δ. Although this method further reduces the reactive power under ZVS operation, it still does not take into account the effect of mutual inductance.

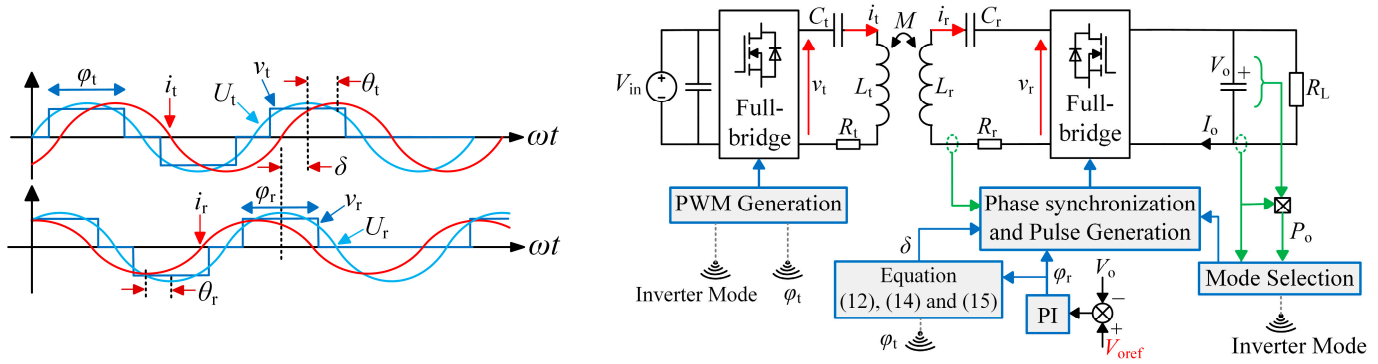
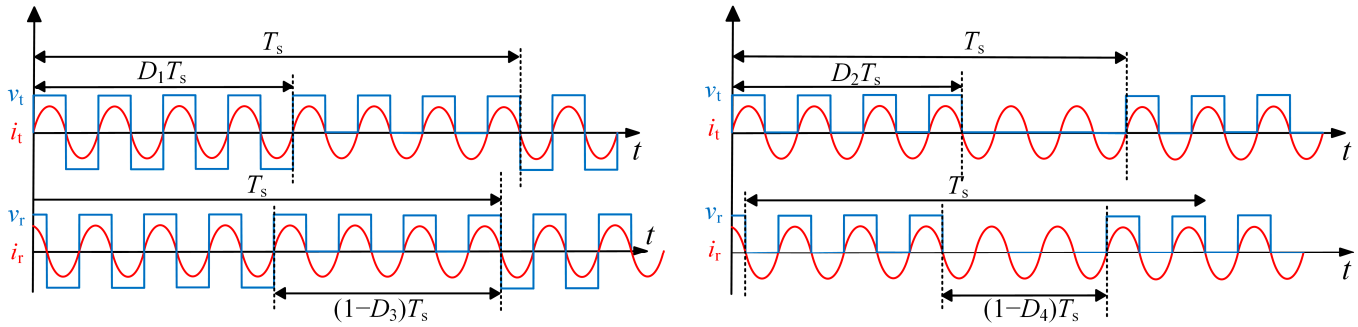


Figure 18. An enhanced mode-switching strategy [62]: (**a**) operating waveforms of the inverter and rectifier working in the mixed-bridge mode; (**b**) system control block diagram.

Jiang et al. [63] perform mode switching only on the transmitter side, simplifying the complexity of control. The receiver-side samples V_o and I_o adjusts φ_r through the PID controller to achieve CVO or CCO, and they control θ_r via a PLL circuit to achieve ZVS. The inverter output voltage U_t on the transmitter side always maintains a full duty cycle and operates in FB mode when the system is heavily loaded, in MB mode when it is half loaded, and in HB mode when it is lightly loaded. The switching method is IM conditioned by the maintenance of V_o and φ_r information received from the wireless communication.

On–Off Keying (OOK) modulation regulates the transmission efficiency by putting the output voltage in FB mode or Zero Output Mode (ZOM) [64], which also belongs to the mode-switching control. Ref. [65] applied OOK to a DSC–MCWPT system to realize

dual-side-enhanced OOK modulation. As shown in Figure 19a,b, the transmitter side or the receiver side operates at FB for a period of time D_1T_s and at HB for another period of time $(1 - D_1)T_s$ in each operating period T_s, called FH mode. It is also possible to operate at HB for a period of time D_2T_s and at ZOM for another period of time $(1 - D_2)\ T_s$, called HZ mode. The system has a total of four operating modes, FH–FH, HZ–HZ, HZ–FH, and FH–HZ. The switching method is used to calculate R_L by sampling V_o and I_o to determine which operating mode can satisfy the IM under the current load to control the AR, and the switching of the transmitter side is based on the information of the receiver side to maintain the CVO; in addition, δ is regulated for realizing the ZVS.



(**a**) (**b**)

Figure 19. Proposed enhanced OOK modulation steady-state operating waveforms of voltage and current [65]: (**a**) FH mode; (**b**) HZ mode.

Although the MSC solves some problems of the TPSC and expands the operating range of the converter's soft-switching, the introduction of both HB and MB modes increases the DC component, which requires a reasonable design of the resonant capacitors and an analysis of the effects brought by the harmonics.

4.5. Asymmetrical Pulse Width Modulation

In light load operation, it is difficult to realize ZVS when the system uses a symmetrical phase shift modulation strategy. Asymmetrical pulse width modulation, also called Asymmetrical Voltage Cancellation (AVC) control, can also be used to improve the efficiency of a conventional DSC–MCWPT system with multi-phase shift control, but in a different way than MSC. As shown in Figure 20a, in the full-bridge operation mode, the lower switching tube of one bridge arm of the bridge converter is always on and the upper switching tube is always off, while the two switching tubes of the other bridge arm are alternately on so that the width of the positive half-wave φ_{t+} is not equal to the width of the negative half-wave φ_{t-} in each cycle. Therefore, the output voltage waveforms are asymmetrical, as shown in Figure 20b,c. The control variables of the system are φ_t and φ_r, where $\varphi_t = \varphi_{t+} + \varphi_{t-}$ and $\varphi_r = \varphi_{r+} + \varphi_{r-}$. The advantage of AVC is that it has a larger pulse width than TPSC and DPSC for the same output power level, which can effectively reduce the reactive power while achieving ZVS.

Ref. [66] proposes a dual-side AVC strategy with the system control structure shown in Figure 21. The control degrees of freedom are φ_t, φ_r, θ_r, K_t, and K_r. The receiver side samples V_o and I_o and uses PI control to meet the desired output and acquires V_{in} for calculating T_{ac} through wireless communication; the phase of i_r is detected by the ZCD circuit. To satisfy the IM and ZVS conditions, the receiver-side controller calculates the phase shift angles φ_{tref} and φ_{rref} and the ZVS angle φ_{rzvs}, which can realize IM under the current operating conditions to control the AR. The transmitter side controls T_{ac} synergistically by acquiring φ_{tref} via wireless communication to regulate the RMS value of U_t. In addition, the authors, in order to extend the range of IM, make the system work in HB mode at light loads. The method synthesizes AVC, TPSC, and MSC and is able to achieve both boost and

buck outputs while verifying proper operation under different coupling coefficients and loads. However, no experimental verification of dynamic switching is performed.

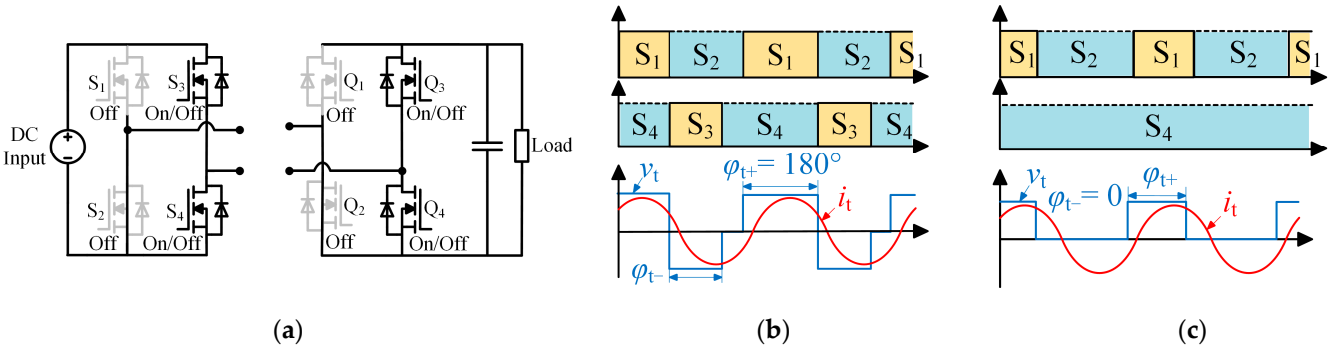


Figure 20. Asymmetrical pulse width modulation: (**a**) switches operating status; (**b**) inverter full-bridge operation waveform; (**c**) inverter half-bridge operation waveform.

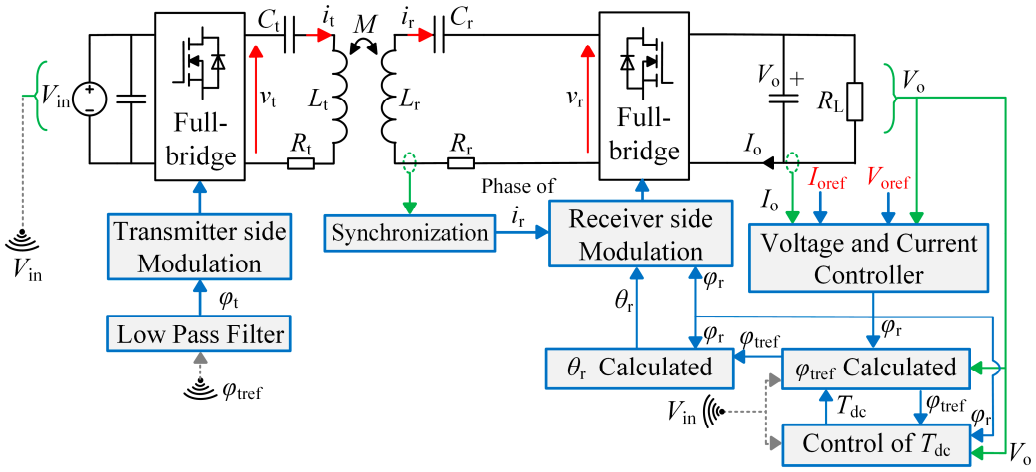


Figure 21. Block diagram of proposed dual-side AVC control [66].

Ref. [67], on the other hand, incorporates a harmonic power transmission strategy based on AVC. Since the voltage waveform of the AC side of the full-bridge converter contains a large number of harmonics when the phase shift angle of the converter is small, the higher harmonics can be used to transmit the power. The authors propose to utilize even harmonics for power transfer called asymmetrical pulse width modulation with an even harmonics strategy. The receiver side samples the output current I_o and compares it with the reference value I_{oref} for PI control and calculates φ_r and δ in order to obtain the desired output power. The transmitter side obtains the information from the communication and realizes the IM by controlling φ_t. And when the output power is less than 1/4 of the rated power, the operating frequency f_s of the system is changed to half of the resonant frequency f_0, and thus, it switches from fundamental to second harmonic power transmission. However, there is a large turn-off current loss under harmonic transmission.

While asymmetrical pulse width modulation optimizes the efficiency when implementing ZVS, it may allow for uneven thermal losses on the switch, as well as higher resonant loop currents.

4.6. Phase Shift Control Strategy Based on Optimal Algorithm Control

Different from the traditional PID or PI algorithm, the Optimal Algorithm Control (OAC), with the help of the numerical computation capability of the controller, takes the realization of optimal efficiency and desired output characteristics as the control objective and is able to adaptively adjust the control variables such as duty cycle, pulse width,

and phase shift angle, which not only improves the dynamic response capability but also improves the robustness of the system. One of the more commonly used ones is the Perturbation and Observation (P&O) algorithm, the basic flow of which is shown in Figure 22. By continuously applying perturbation to the controlled quantity x, if an increase in the controlled object y is observed, the controlled quantity continues to be perturbed in the same direction the next time; conversely, if the transmission efficiency decreases after the perturbation, it is perturbed in the opposite direction the next time. Some DSC methods based on OAC require adding additional DC/DC converters on both sides [68–71], regulating the input voltages and equivalent loads by perturbing the duty cycle of the dual-side DC/DC converters, and exchanging information about the efficiency variations through bilateral communication. The dual-side DC/DC converters undoubtedly increase the cost and complexity of the whole system, and the use of a DAB structure seems to be a better choice.

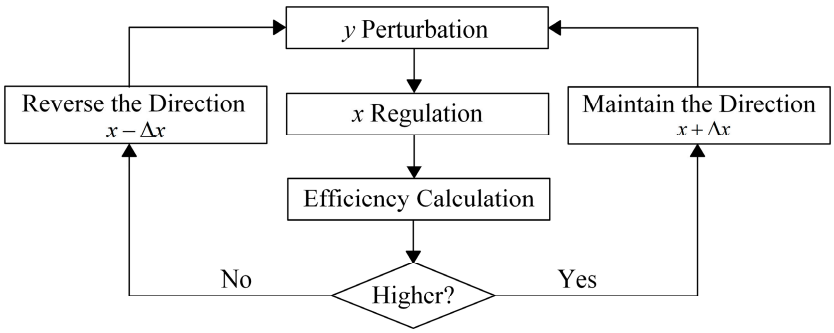


Figure 22. P&O algorithm control flow chart.

Yang et al. [42] used OAC to achieve MEPT in order to realize IM, and the flowchart is shown in Figure 23. The transmitter-side controller makes φ_t decrease from 180° according to the optimal algorithm, records the value of φ_t after each change, and obtains the information of φ_r in real time through wireless communication until $\partial(\sin(\varphi_t/2))/\partial(\sin(\varphi_r/2))$ is equal to some constant, the system achieves IM, and the receiver side realizes the CVO by using the PI control to adjust the φ_r of the SBAR. This method reduces the computational complexity but does not realize ZVS.

In addition, Model Predictive Control (MPC) is used to improve the dynamic response of the DSC due to its unique characteristics. Figure 24a shows the basic flowchart of MPC, whose core idea is to predict and then control, firstly estimating the state quantity y_k of the system within the sampling time kT_s and applying the input quantities u_k, u_{k+1}, u_{k+2}... to obtain the state quantities y_k, y_{k+1}, y_{k+2}. . ., i.e., optimizing the output according to the dynamic model and cost function. And in the next sampling time $(k + 1)T_s$, the prediction window moves with time to achieve rolling optimization, i.e., feedback correction is achieved. The advantages of the MPC are that there is no overshooting compared to traditional PID control and it is a multivariable controller, making it easy to provide a fast dynamic response for multivariable systems.

Liu et al. [72] proposed a MEPT method combining P&O and MPC to improve the dynamic performance of the system. The authors first established a dynamic model of the system output voltage based on the time domain equations, which enabled the receiver side to control not only the output voltage by adjusting φ_r but also the amount of change in the output voltage. The system structure is shown in Figure 24b. The receiver side uses the MPC-based PSC to control φ_r. The CVO is realized by the established prediction model and cost function. In order to realize MEPT, the transmitter side utilizes the P&O algorithm to track the minimum input current I_{in}, and if the current perturbation $\Delta\varphi_t$ decreases I_{in}, which represents that the system efficiency is increasing, the direction of the perturbation is maintained the next time. Meanwhile, the output voltage V_o is sent to the transmitter side, and if the current perturbation $\Delta\varphi_t$ puts V_o in the rated output range, the direction of the perturbation is maintained the next time. This control strategy significantly reduces the

stabilization time of the output voltage. However, it requires the use of multiple sampling circuits, which may subject the steady-state operation to the effects of disturbances.

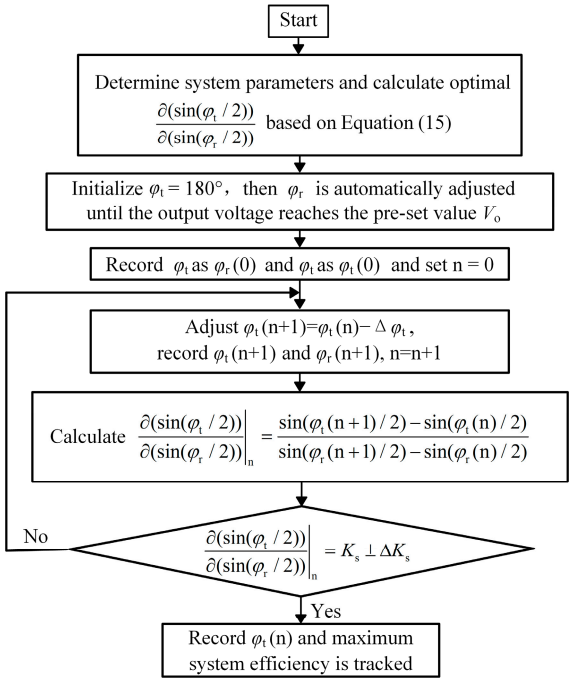


Figure 23. Flowchart of the proposed MEPT control [42].

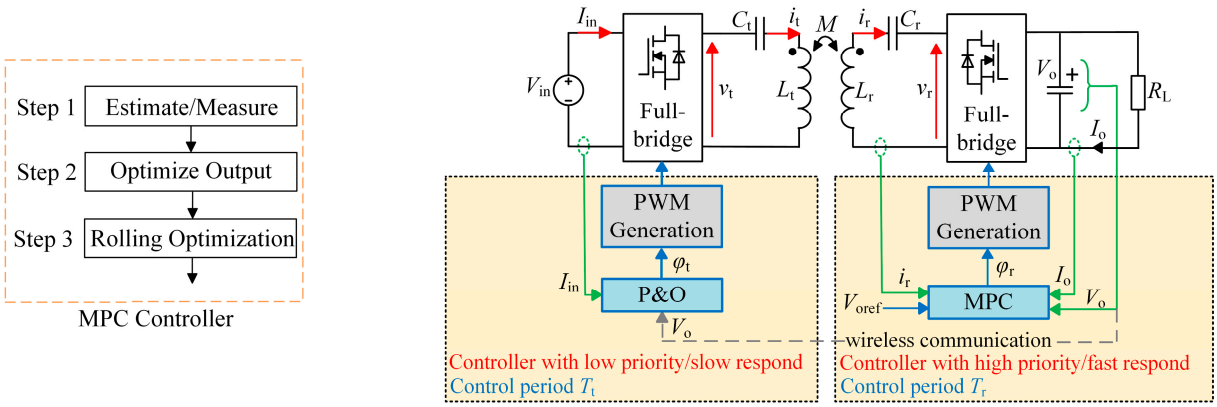


Figure 24. A dynamic improvement of the DSC method using MPC [72]: (**a**) flowchart of MPC; (**b**) block diagram of the proposed control scheme for the system.

Therefore, Chen et al. [36,73] built a linear Expanded State Observer (ESO), i.e., a replica of the dynamic model of the circuit using the system parameters to observe the current, eliminating the need for a current sampling sensor, which can be used to predict the output voltage. The diagram of the improved system is shown in Figure 25, where the receiver-side control maintains the load-side CVO through the Finite-Control-Set Model Predictive Control (FCS-MPC). However, since the general MPC requires multiple rolling calculations, this paper accelerates the convergence of the cost function J_1 through a two-step method and adjusts the step size by a weighting factor Δ_{adp} in the second step if the deviation of the actual voltage from the target voltage decreases. The transmitter side tracks the minimum input current I_{in} using the P&O algorithm, and an adaptive perturbation step method is also proposed to reduce the computation. In the tracking phase, the perturbation step size should be increased to ensure fast convergence to the maximum efficiency, whereas

in the oscillation phase, where the I_{in} changes are small, the perturbation step size should be reduced. The strategy further improves the dynamic performance with improved MPC and P&O and reduces the cost due to reduced sensor usage.

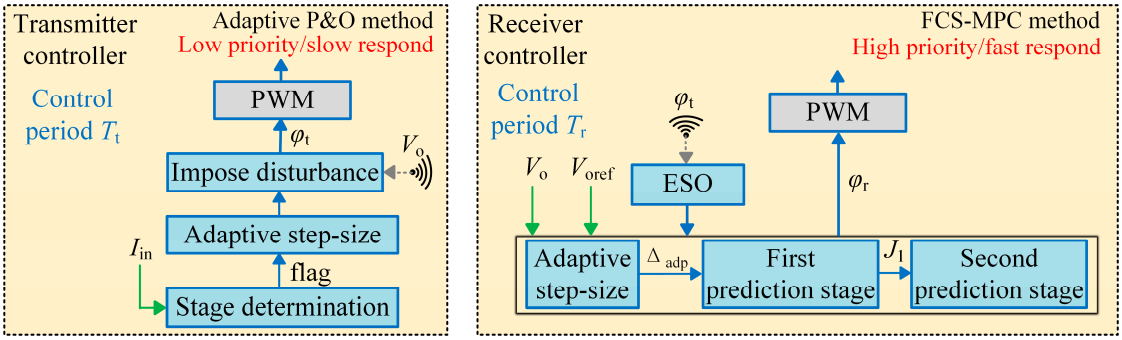


Figure 25. Proposed novel control diagram using Finite-Control-Set Model Predictive Control (FCS-MPC) and Perturbation and Observation (P&O) method [36].

Ref. [74] used the Fuzzy Logic Control (FLC) algorithm to optimize the reactive power loss under different loads, improved dynamic performance due to controlling the converter through the fuzzy rule base, and bilaterally used Pulse Density Modulation (PDM) to implement the ZVS for all the switches. The introduction of PDM will be placed in the next section. In addition, Zhu et al. [75] proposed a parameter identification method in which the rectifier output is short-circuited during the identification process, the frequency is adjusted through a dynamic frequency approximation strategy, the RMS values of the resonant currents of both sides are recorded at different operating points, and finally, the identification of all resonant parameters and mutual inductance of the SS type resonant topology is accomplished through the heuristic algorithm JAYA. After which, the operating frequency of the system's transmitter side tracks the resonant frequency to minimize the reactive power and maintain a constant phase shift angle, while the receiver side receives the identified parameter information through wireless communication, and impedance tuning is achieved through PSC to minimize the reactance.

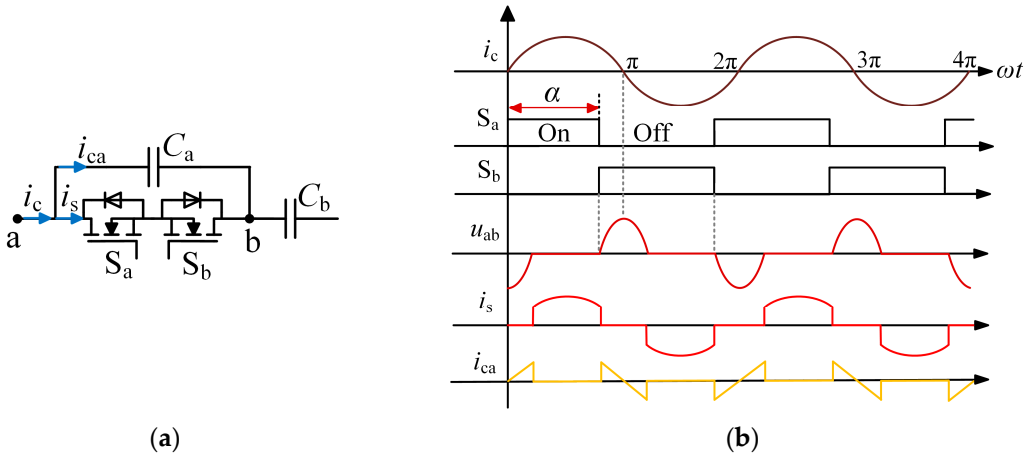
Although the OAC has better dynamic performance, it undoubtedly increases the computational burden of the controller, and the collaboration of DSC algorithms must be considered and the simultaneous adjustment of the phase shift angle should be avoided as much as possible. The constant output should usually be prioritized, and the regulation period of φ_t should be set to be much larger than that of φ_r.

4.7. Tuned Element-Based Phase Shift Control Strategy

In reality, due to aging and tolerances of the components, the capacitors and inductors may undergo parameter drift, resulting in a deviation from the intrinsic resonant frequency of the system. A Switch-Controlled Capacitor (SCC) can adjust the value of the resonant capacitance without the need for complex circuit structures. SCCs usually consist of a parallel capacitor C_a, a series capacitor C_b, and two N-channel MOSFETs connected in series in the reverse direction, which can be switched bi-directionally by PWM to change the equivalent capacitance value, thus adjusting the intrinsic resonance conditions of the system and keeping the system always working in a resonance state.

The SCC and its operating timing diagram are shown in Figure 26a,b. The driving pulse of the switch S_b differs by an angle α from the zero-crossing point of the sinusoidal current i_c with a duty cycle of 0.5, while the driving pulse of S_a is complementary to S_b. During 0-α, parameter u_{ab} is zero because S_a conducts, S_b turns off, and i_c flows through the anti-parallel diodes of S_a and S_b. Until S_a is off and S_b is on, i_c flows through the capacitor C_a and charges C_a to π. And as i_c enters the negative half cycle from π, i_c flows through the anti-parallel diodes of S_a and S_b, C_a discharges, and parameter u_{ab} is always 90° out of phase with i_c, which makes it a variable capacitor whose size is related to the pulse width

α. The equivalent capacitance C_{xeq} of the SCC with respect to C_a, C_b, and α is given in Refs. [76,77].



(**a**) (**b**)

Figure 26. SCC: (**a**) typical SCC structure; (**b**) operation waveforms of the SCC.

Ref. [76] uses dual-side SCC and AVC control methods to achieve efficiency optimization with mutual inductance online estimation. The system structure is shown in Figure 27. The transmitter side adjusts the equivalent capacitance C_{teq} of the SCC by controlling α_t, while the phase shift angle φ_t is adjusted by using the AVC to minimize the reactive power loss while adjusting the operation of the switch ZVS. The receiver side controls α_r to adjust C_{req} to eliminate the reactive component and changes the equivalent load to realize IM by adjusting the phase shift angle φ_r through AVC to ensure that the receiver side is in resonance. However, constant output is not realized and real-time wireless communication is required to achieve a mutual inductance estimation.

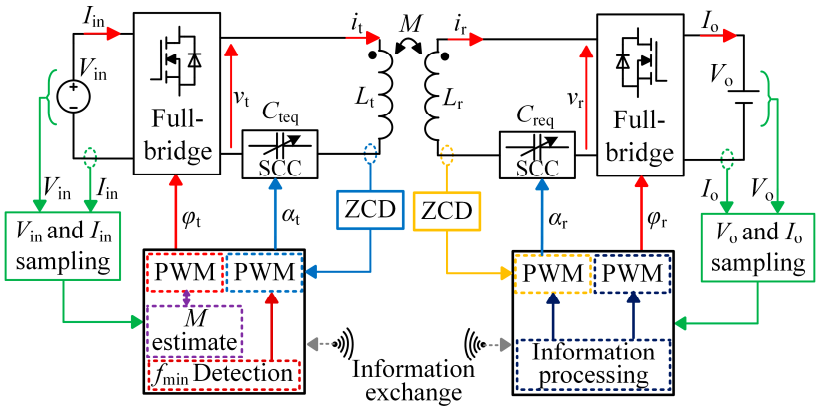


Figure 27. Proposed dual-side SCC and AVC strategy [76].

In order to extend the range of ZVS and reduce the cost associated with SCC, Ref. [77] employs SCC control only on the transmitter side, which achieves converter ZVS while minimizing reactive power losses and decoupling between the ZVS control and the power control loop. The receiver side maintains a CVO through PI control and transmits the phase shift angle φ_r and load information R_L to the transmitter side through wireless communication. By analyzing the time domain model of the circuit, the equations of C_{teq}, φ_t, and φ_r versus R_L for the purpose of achieving constant DC voltage ratio T_{dc} and ZVS on the transmitter side are derived, and a look-up table is made by combining the system parameters to reduce the amount of computation during operation. The transmitter side controls φ_t and SCC to maintain ZVS operation over the full load range according to the look-up table. Compared to the dual-side SCC strategy that realizes both IM and ZVS, the efficiency is improved at a light load, although the efficiency is reduced at rated power. In

Ref. [78], the IM and ZVS are then realized by controlling the optimal external phase shift angle by combining the TPSC and the transmitter-side SCC control.

Ref. [79] proposed a MEPT scheme for load and coupling coefficient variations to achieve CPO and a wide range of IM, and the system structure is shown in Figure 28. Since the SBAR cannot be equated to a pure resistor in realizing IM, the resonant reactance X_r is offset by adjusting the SCC on the receiver side in order to ensure that the total reactance X_{rt} is always zero. And IM is realized not by directly adjusting the equivalent load R_e but by adjusting the resonant current ratio $T_i = I_t/I_r$. The receiver side realizes IM by controlling the phase shift angle through PI, for which the RMS value of the resonant current I_t is sampled and transmitted to the receiver side through wireless communication. The transmitter side regulates the operating frequency by VFC, calculates the output power by obtaining the sampled V_o and I_o of the receiver side according to the wireless communication, and utilizes the PI to control the output power to remain constant under different coupling coefficients and load conditions.

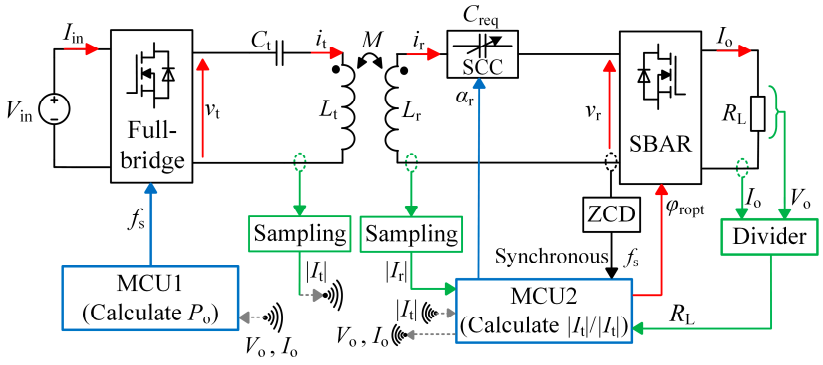


Figure 28. Proposed transmitter-frequency-tuning and receiver-impedance-matching strategy [79].

In addition, a Variable Inductor (VI) is also used in DSC as an adjustable resonant element. As shown in Figure 29, the inductor L_p connected to the main circuit is wound on the center post of the core, while the auxiliary inductor is wound on the two side posts. VI can be realized by attaching an auxiliary circuit and by controlling the output DC current I_{mux} of the auxiliary circuit, and the inductance L_p of the center post will also be changed. Ref. [80] uses VI on the transmitter side to multistage the CCO, while the SBAR on the receiver side optimizes the efficiency by implementing ZVS through PSC.

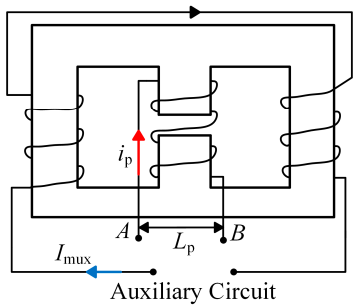


Figure 29. Variable inductor [80].

4.8. Comparison of DSC Strategies with Wireless Communication

In order to compare the DSC–MCWPT with communication control strategies based on DAB converters presented in this section, the control methods, dynamic performance, control objectives, output, and coupling coefficient ranges of each paper are summarized in Table 2, and whether they come with mutual inductance estimation or not is listed. If there is a range of output range or coupling coefficients, it means that the control strategy has load or coupling coefficient-independent performance. Since both constant output and IM

are related to mutual inductance, estimating mutual inductance compensates for possible positional deviations of the coil and improves the robustness of the controller. Although some research experiments give fixed coupling coefficients, offset experiments are still conducted, so they are also listed together.

Table 2. Comparison of control strategies with wireless communication for DSC–MCWPT systems based on DAB converters.

Reference	DSC Methods	Maximum Dynamic Response Time	Efficiency Optimization Methods	Constant Output	Output Range	Coupling Coefficient Variation Range	Estimate of Mutual Inductance
[45]	DPSC	30 ms	IM	CCO/CVO	P_o: 100–1000 W V_o: 150–300 V R_L: 30–200 Ω	0.22, horizontal offset	No
[46]	DPSC, PLL-CTM	140 ms	IM	CCO/CVO	V_o: 30–72 V R_L: 8–200 Ω	0.15–0.2	No
[47]	DPSC	Not mentioned	IM	CCO	P_o: 0–500 W	0.314	Yes
[50]	TPSC	Not mentioned	IM, ZVS	No	P_o: 200–1021 W V_o: 160–240 V	0.14–0.2	No
[44]	TPSC	112 ms	IM, ZVS	No	P_o: 300–1500 W V_o: 150–400 V	0.275	No
[51]	TPSC	130 ms	IM, ZVS	CPO	P_o: 120 W V_o: 55–78 V	0.243–0.271	Yes
[52]	TPSC	300 ms	ZVS	CCO/CVO	P_o: 45–320 W V_o: 30–80 V R_L: 8–200 Ω	0.1–0.2	No
[53]	TPSC	250 ms	IM	CVO	P_o: 300–800 W V_o: 120 V R_L: 20–30 Ω	0.186	No
[54]	VFTPSC	Not mentioned	IM, ZVS	No	P_o: 200–1000 W V_o: 160–240 V	0.115–0.312	Yes
[55]	VFTPSC	Not mentioned	IM, ZVS	CPO	P_o: 200–1000 W V_o: 400 V	0.08–0.29	Yes
[56]	VFTPSC	Not mentioned	ZVS	CCO/CVO	P_o: 200–1200 W V_o: 100–200 V R_L: 16.67–33.33 Ω	0.25–0.62	No
[57]	VFC, PSC	2 ms	Minimum power angle	No	R_L: 50 Ω	0.2	No
[58]	VFC, PSC	20 ms	IM, ZVS	CCO	V_o: 20–100 V I_o: 2A	0.294	No
[59]	MSC	Not mentioned	IM	No	P_o: 58–1000 W V_o: ≈130 V R_L: 16–200 Ω	Not mentioned	No
[60]	MSC, DPSC	Not mentioned	IM, ZVS	No	P_o: 100–800 W V_o: 250–450 V R_L: 16.67–33.33 Ω	0.17	No
[61]	MSC, TPSC	140 ms	IM, ZVS	CVO	P_o: 300–1800 W V_o: 220 V	0.3831	No
[62]	MSC, TPSC	190 ms	IM, ZVS	CVO	P_o: 1–10 kW V_o: 400–600 V	0.14–0.19	No
[63]	MSC, PSC	476 ms	IM, ZVS	CCO/CVO	V_o: 45–90 V I_o: 1–3.5 A R_L: 10–160 Ω	0.15–0.23	No
[65]	OOK	690 ms	IM, ZVS	CVO	P_o: 140–500 W V_o: 200 V	0.198	No
[66]	AVC, PSC, MSC	Not mentioned	IM, ZVS	CCO/CVO	P_o: 82.25–3700 W V_o: 250–375 V	0.1–0.3	No

Table 2. *Cont.*

Reference	DSC Methods	Maximum Dynamic Response Time	Efficiency Optimization Methods	Constant Output	Output Range	Coupling Coefficient Variation Range	Estimate of Mutual Inductance
[67]	APWMEN	Not mentioned	IM, ZVS	No	P_o: 50–1000 W V_o: 275–325 V	0.2	No
[42]	OAC, DPSC	17 ms	IM	CVO	V_o: 72 V R_L: 25–95 Ω	0.15, vertical and horizontal offset	No
[72]	MPC, P&O, DPSC	12 ms	Minimum DC current input	CVO	V_o: 100 V R_L: 50–70 Ω	0.201	No
[36]	MPC, P&O, DPSC	94 ms	Minimum DC current input	CVO	V_o: 260–300 V R_L: 150–900 Ω	0.19–0.24	No
[74]	FLC, PDM	Not mentioned	ZVS	CVO	V_o: 360 V R_L: 35 Ω	0.1–0.4	No
[75]	JAYA, VFC, PSC	Not mentioned	Minimum power angle	No	P_o: 200–800 W	0.22–0.35	Yes
[76]	SCC, AVC, DPSC	Not mentioned	IM, ZVS	No	P_o: 200–650 W	0.12, vertical offset	Yes
[77]	SCC, DPSC	28 ms	IM, ZVS	CVO	V_o: 320–400 V I_o: 3.2–14 A	0.3	No
[78]	SCC, TPSC	Not mentioned	IM, ZVS	No	V_o: 400–800 V P_o: 500–6000 W	0.3	No
[79]	SCC, VFC, PSC	Not mentioned	IM, ZVS	CPO	P_o: 308 W R_L: 30–150 Ω	0.16–0.3	No
[80]	VI, PSC	Not mentioned	ZVS	CCO	I_o: 3–7 A R_L: 5–51.8 Ω	0.27	No

Multiple control objectives and good dynamic performance cannot be achieved simultaneously using only DPSC and PI control, and it is difficult to achieve ZVS. TPSC is able to achieve both ZVS and IM by introducing additional control variables. However, the general constant frequency TPSC is unable to achieve multiple control objectives and tolerance under load and coupling coefficient variations at the same time. The VFTPSC improves the robustness of the control strategy by frequency tuning, but the variation of the operating frequency affects the output ripple and dynamic performance of the system. To further optimize the efficiency, a multi-phase shift control strategy combined with mode-switching control is proposed, but it may lead to poor dynamic performance. The asymmetric pulse width modulation strategy also improves the TPSC and reduces the large reactive power losses introduced by realizing the ZVS, but its dynamic performance has not been fully investigated. In contrast, control algorithms such as MPC and FLC can also improve dynamic performance through the implementation of OAC optimization efficiency independent of parameter variations and mutual inductance estimation. SCC and VI can be used for tuning to improve tolerance to parameter variations of the resonant elements but require more attention to dynamic performance.

Obviously, different control methods can be combined with each other to form new control strategies. MSC and AVC are mostly used to achieve ZVS. MPC is used to maintain the constant output. The P&O algorithm can be used to achieve both a constant output and MEPT. The VFC method can also be used to control the constant output power or to change the equivalent impedance, but the impedance at different frequencies will not be comparable. Adjusting the SCC and VI can then be used to change the resonance conditions so that the system achieves the necessary conditions to realize ZVS and IM.

However, since the DSC–MCWPT system operates at high frequencies, the reliability of the wireless communication link can be disturbed by electromagnetic noise, and continuous perturbations may affect system stability and reduce system efficiency, especially for optimized control strategies that require the exchange of information between the

transmitter and receiver sides. The existence of time delay in communication may lead to the deterioration of the dynamic response of the system.

5. Control Strategies Without Wireless Communication for DSC–MCWPT Systems Based on DAB Converters

The non-communication DSC method can achieve constant output only through TSC or RSC without the help of communication feedback, and then optimize the system efficiency through the converter on the other side [81], which not only improves the reliability of the system but also reduces the cost of the communication link.

5.1. Non-Communication Phase Shift Control Strategy Based on Phase Detection

The DPSC and TPSC methods based on wireless communication were introduced in the previous section, while the wireless communication link can be omitted under specific efficiency optimization strategies; however, phase detection circuits are generally required to accurately and reliably obtain the phase of the resonant current, and the commonly used methods are ZCD and PLL.

A non-communication DPSC and mutual inductance estimation method is proposed in Ref. [82]. First, the results of the mutual inductance M and self-inductance parameters of the designed coil with distance are simulated and made into a look-up table. The transmitter side estimates the M by calculating the magnitude and angle of the input impedance, and the junction and look-up tables verify the corresponding self-inductance values, while the operating frequency at this point is higher than the intrinsic resonant frequency at maximum offset. After that, the system operates at the resonant frequency, and the receiver side maintains the synchronous rectification control to keep the output voltage constant by controlling the phase shift angle φ_r through PI. On the other hand, the transmitter side estimates the voltage U_r by sampling the RMS value of the resonant current and adjusts the phase shift angle φ_t so that U_r is constantly equal to U_t, which can balance the current stresses on both sides, which is equivalent to the realization of IM and optimizes the efficiency of the system to a certain extent.

Iam et al. [83] designed the control system of Figure 30 in order to realize CCO/CVO charging and ZVS while eliminating the wireless communication. During the CCO charging process, the load-independent CCO-charging characteristic of the SS resonant topology under full positive pairing is utilized to keep both sides of the converter operating at full phase shift angle. And when the system is switched from CCO to CVO operation, the receiver side maintains a CVO through the PI control of the SBAR. However, the decrease of the phase shift angle of the SBAR in realizing ZVS and CV control will increase the equivalent load reactance X_e and generate reactive power loss. In order to improve the system efficiency, the transmitter side controls the phase shift angle φ_t according to the magnitude of the power angle θ_t by means of a phase detection circuit PLL, which avoids the drastic change of φ_t due to the adjustment of the output voltage by φ_r. However, the control structure of PLL combined with PWM is complicated.

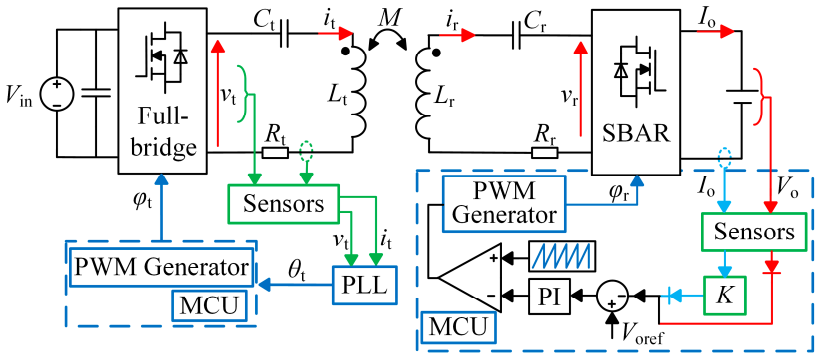


Figure 30. Proposed non-communication DPSC system [83].

Liu et al. [84] sampled the phase of the resonant current through a phase detection circuit, and the active full-bridge rectifier on the receiver side operates by turning one side's switches off all the time while letting the other side's switch realize the PSC with its body diodes, realizing the CVO through PI control and adjusting the power angle θ_r to ensure the zero-current shutdown of all the body diodes and the ZVS turn-on of the lower switches. The transmitter side maintains the minimum ZVS angle by adjusting the phase shift angle φ_t according to the power angle θ_t.

In order to use AVC in non-communication DSC–MCWPT, it is stated in Ref. [85] that the phase angle of the control should be associated by only one control degree of freedom, so the system is more suitable to use a half-bridge converter where the receiver side carries out the precise regulation of the output voltage and the PLL controller is used for the phase detection so that the system maintains the ZVS operation, and the transmitter-side controller is slowly varied with the load changes to avoid, as far as possible, the asymmetry of the resonant currents on both sides, optimizing the efficiency as well as improving the phase locking capability so that the efficiency at a light load is improved.

However, it is difficult to realize the control of the external phase shift angle δ with the non-communication DSC strategy based on phase detection. Ref. [86] estimates the phase of the resonant current on the transmitter side by adding an auxiliary winding on the receiver side, and thus controls δ to achieve a bi-directional transmission of power, but the transmitter only maintains constant output control and fails to optimize the efficiency further. Zhang et al. [40] optimized the system efficiency by adding drive windings and driving circuits on both sides and regulating δ by the phase difference between the voltages of the active converter and the drive winding but failed to achieve DSC.

5.2. Non-Communication Dual-Phase Shift Control Based on Optimal Algorithm Control

Since OAC such as P&O do not rely on sampling, computation, and circuit parameters, non-communication MEPT can be realized by tracking the input or output current and voltage. However, it is difficult to judge the stability of the control scheme due to the lack of feedback information on the other side, bringing about poor MEPT accuracy.

Ref. [87] realizes IM and CVO via non-communication DPSC, and the system structure is shown in Figure 31. The receiver-side controller puts v_r and i_r in phase to keep the equivalent load purely resistive and realizes the CVO by PID, controlling the phase shift angle φ_r according to the reference value of the output voltage under different loads. And under constant DC input voltage and mutual inductance, the operating point for realizing IM is a monotonic function of φ_r, φ_t, and load resistance. In order to reduce the control difficulty, the transmitter side can realize IM by tracking the maximum efficiency point by adjusting the phase shift angle φ_t to keep the DC input current I_{in} as a minimum value through the P&O algorithm.

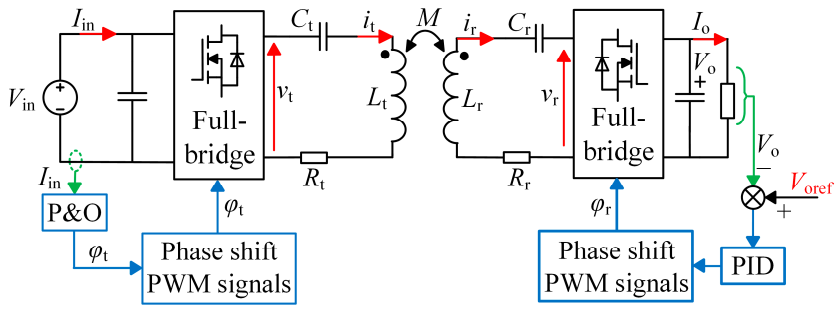
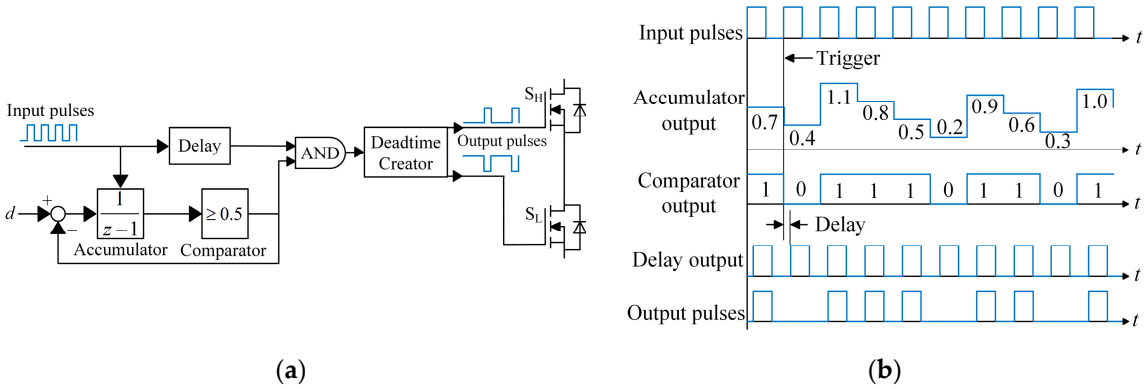


Figure 31. Proposed non-communication DPSC based on P&O [87].

Similarly, Li et al. [88] realized MEPT using P&O-based PSC tracking minimum I_{in} on the transmitter side and PI-controlled SBAR phase shift angle φ_r on the receiver side to achieve CCO to supercapacitors.

5.3. Non-Communication Pulse Density Modulation Control Strategy

Pulse Density Modulation (PDM), as an alternative solution to PWM, is able to solve the problem of soft-switching that is difficult to achieve with conventional DPSC. The control degree of freedom of PDM is the pulse density d, which refers to the ratio of the number of remaining pulses to the total number of switching cycles and is capable of controlling the power flow and the equivalent load. The driving pulse of the PDM can be precisely generated by a Delta–Sigma Modulator (DSM) to control a half-bridge converter, for example. As shown in Figure 32a, the controller takes every ten switching cycles as a modulation period, and while the duty cycle of the input pulse is fixed at 0.5, the comparator output and the set pulse density perform error operation and send it into the accumulator. The accumulator is triggered every time the input pulse reaches the rising edge and the result of the accumulation is sent into the comparator, and finally, the comparator output and the delayed input pulse are used to generate the actual pulse signals by the and operation so that the converter's output pulse in a switching cycle is diluted. According to the principle of volume–density balance, the actual output voltage RMS of the PDM will be d times the original. The modulation waveform at $d = 0.7$ is shown in Figure 32b.



(**a**) (**b**)

Figure 32. PDM [89]: (**a**) PDM of half-bridge converter based on a Delta–Sigma modulator; (**b**) waveforms of the modulator when $d = 0.7$.

Li et al. [89] realized dual-side PDM control and proposed a soft-switching technique for load variations. The system structure is shown in Figure 33. The transmitter-side PDM pulses are generated directly by the controller, and the ZVS is achieved by adjusting the pulse density d_t to achieve a CVO and keep a small power angle θ_t. The receiver side requires the synchronization signal generated by i_r to be the input pulse of the PDM, and the ZVS and IM are achieved by adjusting the pulse density d_r. This method realizes non-communication CVO, ZVS, and IM over a wide load range with dual-side PDM. However, the smaller pulse density introduces a larger output voltage ripple and lacks complete closed-loop control.

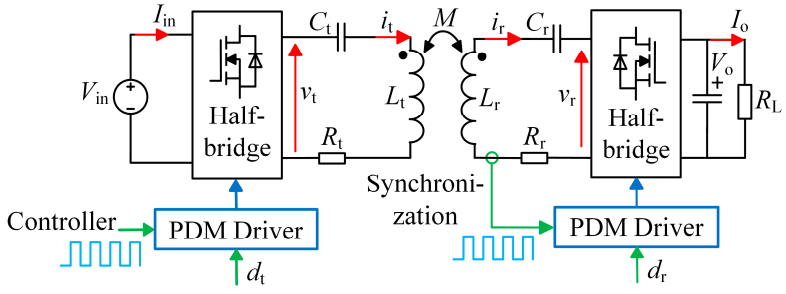


Figure 33. Proposed PDM implementation for MEPT [89].

Chen et al. [90], on the other hand, optimized efficiency using PDM control on a single side only. The receiver side uses the PID control of the power angle θ_r to regulate the output voltage, but θ_r is too large to reduce the efficiency and power factor. The transmitter side reduces the input voltage by regulating the power angle θ_t through PDM to maintain θ_r at a small value while ensuring that the CVO is realized. And soft-switching can also be realized by regulating θ_t and θ_r. Ref. [91], on the other hand, only uses PDM on the receiver side to realize the identification of inductive and capacitive parameters and only performs frequency control on the transmitter side without additional wireless communication modules, which can ensure the resonant operation of the receiver side under parameter drift and coupling variation.

To further realize ZVS with variable coupling coefficients and loads, Ref. [92] uses a full-bridge converter with dual-side PDM control. The current for the realization of ZVS is provided by a well-designed series resonant branch. Due to the presence of negative voltage, the pulse density d at this point represents the total density of positive and negative pulses. The d_t and d_r on both sides are regulated by the controller to be able to achieve the desired output voltage and efficiency optimization, respectively. And to ensure the stable operation of the system, the rules for generating the pulse train are developed. However, PDM requires high-quality factor coils and is prone to low harmonics.

5.4. Non-Communication Frequency-Modulated Phase-Shift Keying Control Strategy

Wireless communication methods usually require specialized modules or auxiliary circuits, which undoubtedly reduce the reliability of system operation. Phase-Shift Keying (PSK) converts the phase difference between the resonant voltage and resonant current on one side into a digital signal by means of the phase characteristic Equation (8) during resonance matching, which is continuously adjusted at a certain rate, while the desired phase information is obtained by demodulation on the other side. PSK can be used for synchronous rectification of Active Rectifiers [93] to reduce the interference of wireless communication on power transmission.

Ref. [94] proposes the Frequency-Modulated Phase-Shift Keying (FMPSK) method, where the frequency-modulated transmits equivalent information at the rate of kb/s by updating the phase change within each phase shift cycle T_{PSK}. The system structure is shown in Figure 34, where the receiver-side current i_r generates the synchronization signal i_{r1} via ZCD and PLL, and the PI and PDM controls are used to adjust the pulse density d_r to regulate the DC output voltage V_o and to change the power angle θ_r via a phase shifter for realizing soft-switching. The transmitter side also generates a signal i_{t1} in phase with the current i_t via ZCD and PLL and generates the drive signal for the switches at a fixed frequency. Power angle θ_t is obtained by detecting the phase difference between the v_t and i_t, demodulating the information of θ_r according to Equation (8), and finally adjusting the pulse density d_t by PDM to realize IM. However, the continuous regulation of θ_r causes fluctuations in the output power. Ref. [95] reduces the fluctuations in the output power by regulating the pulse density d_r through the PDM at the receiver side, and the transmitter side receives the information through the FMPSK and controls the output power using the PDM.

Since the MEPT process is affected by mutual inductance, Ref. [96] proposes a non-communication coupling coefficient identification method, which does not require complex modeling and can be quickly and dynamically identified by the logic function of the hardware alone. First, a command is passed from the transmitter side to the receiver side via FMPSK to short-circuit the AR to operate. The transmitter side samples the RMS values of the input voltage v_t and the resonant current i_t, and according to the relationship between the input impedance Z_{in} and the frequency and the coupling coefficient, by sweeping f_s from the minimum value of f_{smin} to the maximum value of f_{smax}, or sweeping f_s from the maximum value of f_{sma} to the minimum value of f_{smin}, then the operating frequency that makes Z_{in} purely resistive will be found; at this time, $\mathrm{Im}(Z_{in}) = 0$, and the coupling coefficient at the current operating state will be found according to the formula.

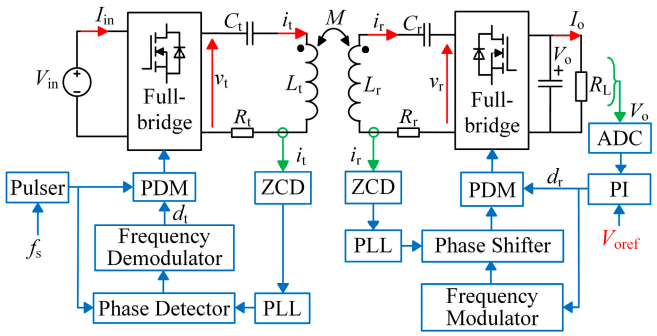


Figure 34. Proposed DSC–MCWPT system using FMPSK communication for MEPT [94].

The above methods achieve only unidirectional information transfer. Ref. [97] proposes FMPSK communication capable of bi-directional demodulation with a smaller amount of phase modulation to reduce the impact on output fluctuations, but without further optimizing the efficiency of the system.

5.5. Non-Communication Tuned Element-Based Phase Shift Control Strategy

Although soft-switching [76] and frequency tuning [79] via PWM-controlled SCC have been proposed in this paper, both require wireless communication leading to a number of problems such as slower control speed and lower robustness. Ref. [98] proposes non-communication dual-side VI control capable of achieving CPO with high power factor under coil offset, with the control variables being the transmitter-side inductance L_t and the receiver-side inductance L_r. Inductance L_t is used to provide the ZVS condition under misalignment, and inductance L_r regulates the output power, but the bridge converter with two sides has not been realized to be efficiently utilized.

Rong et al. [99] proposed a DSC–MCWPT system based on Fractional Order Element (FOE), as shown in Figure 35. This method uses the coupled mode theory in physics to analyze the transmission characteristics of the system. The ZPA control on the transmitter side operates whether it works in CCO or CVO mode according to the input power. The transmitter side provides different operating frequencies and phase shift angles under different charging modes, and the power converter on the receiver side is controlled as a Fractional Order Element. Parameter Z_v is the equivalent fractional impedance, where $Z_v = R_v + jX_v$, and parameter v is the order, which is linear with the power angle θ_r. When $-1 < v < 0$, the fractional element has positive resistance and capacitance components. This control strategy adjusts the order v according to different coupling distances and charging states, so that the working frequency of the system automatically tracks the intrinsic resonant frequency. The resonant matching is achieved through dual-side frequency tuning. Compared with the traditional integer order control method, the system improves robustness and tolerance to position the deviation of coils. The fractional element allows for more flexible and adaptive control strategies, especially in systems with nonlinear and time-varying characteristics.

5.6. Comparison of DSC Strategies Without Wireless Communication

Table 3 compares the non-communication DSC methods presented in this chapter. First, we find that most of the non-communicating DSC studies do not perform dynamic experiments, although communication introduces additional delay time. Second, although most of the methods do not have mutual inductance estimation, the non-communication strategy makes the system somewhat resistant to offset, since constant output and efficiency optimization are performed separately.

Non-communication DPSC and TPSC can achieve both constant output and efficiency optimization, but it is difficult to achieve IM and ZVS simultaneously. In contrast, P&O can achieve optimal efficiency by tracking the minimum DC input, but the control accuracy is limited. The PDM strategy can achieve IM and ZVS at the same time, but the output ripple

needs to be optimized. The FMPSK, as a communication strategy, can achieve constant output under a wide range of coupling variations. However, most of them need to work with PDM, which has an impact on the output accuracy. Tuned elements such as VI or FOE can improve the system's offset resistance, but it is difficult to control.

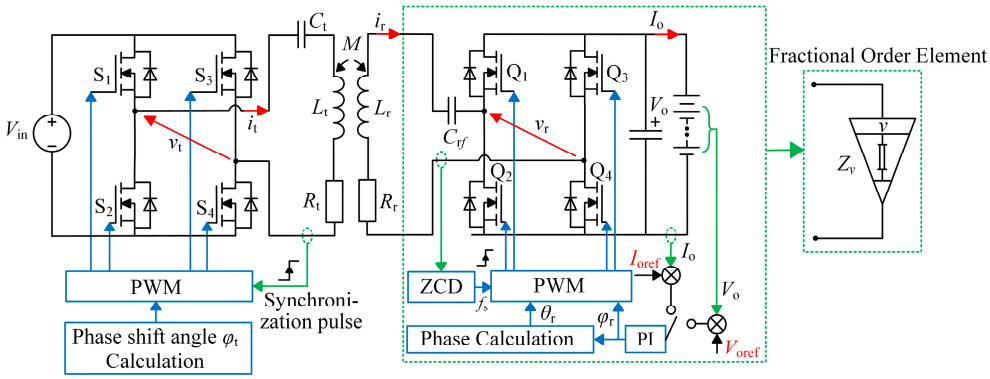


Figure 35. Proposed a DSC–MCWPT system based on Fractional Order Element [99].

Table 3. Comparison of control strategies without wireless communication for DSC–MCWPT systems based on DAB converter.

Reference	DSC Methods	Maximum Dynamic Response Time	Efficiency Optimization Methods	Constant Output	Output Range	Coupling Coefficient Variation Range	Estimate of Mutual Inductance
[82]	DPSC, VFC	Not mentioned	IM	CVO	V_o: 180 V P_o: 36–180 W	0.68–0.78	Yes
[83]	DPSC	20 ms	ZVS	CCO/CVO	V_o: 170 V I_o: 5 A R_L: 0–360 Ω	0.232–0.255	No
[84]	TPSC	Not mentioned	ZVS	CVO	V_o: 20 V P_o: 11.25–90 W	0.2	No
[85]	AVC, PSC	Not mentioned	ZVS	No	V_o: 30–48 V	0.3–0.6	No
[87]	P&O, DPSC	Not mentioned	Minimum DC current input	CVO	V_o: 20 V P_o = 8–16 W	Vertical offset	No
[88]	P&O, DPSC	Not mentioned	Minimum DC current input	CCO	I_o: 3 A	0.15, vertical offset	No
[89]	PDM	Not mentioned	IM, ZVS	CVO	V_o: 33 V R_L: 25–100 Ω	0.01	No
[90]	PDM	Not mentioned	ZVS	CVO	V_o: 40 V R_L: 30–60 Ω	0.11	No
[92]	PDM	Not mentioned	ZVS	CVO	V_o: 31.8 V R_L: 25–100 Ω	0.02–0.23	No
[94]	FMPSK, PDM	1 ms	IM, ZVS	CVO	V_o: 50 V P_o: 25–125 W	0.01–0.1	No
[95]	FMPSK, PDM	Not mentioned	IM	CVO	V_o: 50 V	0.03–0.1	No
[98]	VI	Not mentioned	ZVS	CPO	P_o: 300 W	Vertical and horizontal offset	No
[99]	FOE, VFTPSC	Not mentioned	ZVS	CCO/CVO	V_o: 216 V I_o: 4 A R_L: 45–540 Ω	0.196–0.46	No

6. Comparison of DSC–MCWPT Systems Based on DAB Converters with and Without Wireless Communication

Based on the introduction of various control strategies in the previous two sections, we introduce and compare the wireless communication methods in the control strategies and provide a comprehensive comparison of various DSC methods with and without wireless communication modules in this section.

6.1. Comparison of Wireless Communication Methods

The commonly used wireless communication method in MCWPT is through the RF module, i.e., the electrical information is modulated into a RF signal for long-distance information transmission. Commonly used wireless communication modules such as WiFi, Bluetooth, NFC, and ZigBee are all based on the RF principle, and their comparison is shown in Table 4 below. In Table 4, the maximum delay time and transmission distance refer to the parameters for the system to work properly in an indoor environment.

Table 4. Comparison of RF wireless communication methods.

RF Communication Method	Operating Frequency Band	Maximum Delay Time	Transmission Distance	Power Consumption Class	Latest Communication Protocol
WiFi	2.4 GHz	50 ms	<50 m	High	IEEE 802.11n
Bluetooth	2.4 GHz	100 ms	<10 m	Medium	Bluetooth 6.0
NFC	13.56 MHz	5 ms	<10 cm	Extremely low	IEEE 802.15.1
ZigBee	2.4 GHz	30 ms	<30 m	Low	IEEE 802.15.4

In the DSC–MCWPT system, the commonly used RF modules are the NRF24L01 series [45,47,51,53,61,62] and a 2.4 GHz WiFi module [56,57]. The NRF24L01 module is different from Bluetooth and WiFi in that it has the advantages of high speed, low power consumption, and low cost, and it can limit the communication delay to hundreds of microseconds, so it is widely used. However, the effect of communication delay on frequency regulation and dynamic regulation is still not negligible.

In contrast, bilateral messaging via non-communicational control PSK or FMPSK has the advantages of low cost, simple structure, and high reliability, and it only requires certain configuration of the control chip. However, when the coil is misaligned, it will lead to the instability of communication and signal quality degradation, and the effect of dynamic corresponding delay still needs to be improved.

6.2. Comparison of DSC Strategies

Table 5 compares the DSC–MCWPT systems based on the DAB converter with and without communication. First, the type refers to the power conversion topology combinations presented in Table 1. Then, the same or similar control strategies are compared by putting them together with respect to their control variables and control purpose. The maximum efficiency and output power at a certain operating frequency reflect the optimal operating conditions of the system. Finally, the advantages of each strategy are summarized. Since the length of the table could not be shown on one page.

The most used DSC strategy based on DAB converters is dual-side full-bridge converters topology type I and more kW stage output applications, followed by type II using SBAR, which is also common. The bridge converter is most often used as a PSC, bringing control variable phase shift angles φ_t and φ_r. However, most of the DSC methods use constant frequency control and set the operating frequency to 85kHz to meet the wireless charging requirements for Electric Vehicles. DPSC with communication enables precise phase control and IM, which is difficult to achieve with non-communication DPSC or TPSC. FMPSK-based PDM strategies are similar to TPSC using PWM control and hence are put together for comparison. Although the non-communication methods have high efficiency, they both operate at higher frequencies and have lower output power levels. The dual-side

non-communication PDM strategy is similar to the MSC strategy used to implement ZVS, but the difficulty in optimizing reactive power losses leads to relatively low efficiency. Non-communication OAC methods have lower accuracy and relatively lower efficiency compared to MEPT with communication, but the lack of need for communication leads to improved robustness. Most of the DSC methods using tuning element SCC require wireless communication.

Table 5. Comparison of the above control strategies.

Reference	Type	Wireless Communication	Control Strategy	Control Variable	Control Purpose	Operating Frequency	Maximum Efficiency	Maximum Power	Advantages
[45]	I	Yes	DPSC	φ_t and φ_r	IM, CCO/CVO	85 kHz	93%	1 kW	Small resonant current loss
[46]	I	Yes	DPSC, PLL-CTM	φ_t and φ_r	IM, CCO/CVO	85 kHz	90.2%	288 W	Precise phase signal generation
[47]	I	Yes	DPSC	φ_t and φ_r	IM, CCO	85 kHz	85%	500 W	Phase synchronization achieved by tracking DC current output
[82]	I	No	DPSC, VFC	φ_t, φ_r and f_s	IM, CVO	97.4–112.56 kHz	83.13%	150 W	Estimation of information on the receiver side only on the transmitter side
[83]	II	No	DPSC	φ_t, φ_r	ZVS, CCO/CVO	50 kHz	94.345%	850 W	Efficiency improvement under non-communicating ZVS
[50]	I	Yes	TPSC	φ_t, φ_r and δ	IM, ZVS	85 kHz	94.83%	1021 W	Soft-switching over a wide load range
[44]	I	Yes	TPSC	φ_t, φ_r and δ	IM, ZVS	85 kHz	93.6%	1500 W	Soft-switching over a wide output voltage range
[51]	I	Yes	TPSC	φ_t, φ_r and δ	IM, ZVS, CPO	50 kHz	87.5%	120 W	Elimination of PI controllers, feasibility of load, and coupling factor variation
[52]	I	Yes	TPSC	φ_t, φ_r and θ_r	ZVS, CVO	85 kHz	96.8%	320 W	MEPT under ZVS conditions
[53]	I	Yes	TPSC, AMC	φ_t, φ_r and θ_r	IM, CVO	30 kHz	91.7%	800 W	MEPT under varying load and detuning conditions
[84]	I	No	TPSC	φ_t, φ_r and θ_r	ZVS, CVO	95.6 kHz	90.3%	90 W	Efficiency is much less dependent on load
[94]	I	No	FMPSK, PDM	d_t, d_r and θ_r	IM, ZVS	1 MHz	93%	125 W	Hardware implementation of compact MEPT with low power flow interference
[95]	I	No	FMPSK, PDM	d_t, d_r and θ_r	IM	1 MHz	91%	25 W	Phase modulation with low output power and voltage fluctuations
[54]	I	Yes	VFTPSC	φ_t, φ_r, θ_r and f_s	IM, ZVS	85–92.3 kHz	94.9%	1000 W	MEPT under large varying load and coupling conditions
[55]	I	Yes	VFTPSC	φ_t, φ_r, δ and f_s	IM, ZVS	79–90 kHz	93%	1000 W	MEPT under large varying conditions
[56]	I	Yes	VFTPSC	φ_t, φ_r, δ and f_s	ZVS	84–87 kHz	95.6%	1200 W	ZVS operation and minimum reactive current over a large range
[57]	II	Yes	VFC, PSC	θ_t, θ_r, δ and f_s	Tuning impedance	85–94 kHz	Not mentioned	50 W	Fast decoupling algorithm under capacitive detuning
[58]	II	Yes	VFC, PSC	θ_r, f_s	IM, ZVS, CCO	Not mentioned	<85%	200 W	Increased charging efficiency for step-up loads
[59]	I	Yes	MSC	K_t, K_r	IM	85 kHz	94.5%	1000 W	IM under large load variations
[60]	I	Yes	MSC, DPSC	φ_t, φ_r, K_t, K_r	IM, ZVS	85 kHz	95.6%	800 W	Wide range soft-switching for optimized efficiency under light load conditions
[61]	I	Yes	MSC, TPSC	φ_t, φ_r, δ, K_t and K_r	IM, ZVS, CVO	85 kHz	94.29%	1800 W	ZVS and loss optimization at light loads, MEPT over wide load range

Table 5. *Cont.*

Reference	Type	Wireless Communication	Control Strategy	Control Variable	Control Purpose	Operating Frequency	Maximum Efficiency	Maximum Power	Advantages
[62]	I	Yes	MSC, TPSC	φ_t, φ_r, δ, K_t and K_r	IM, ZVS, CVO	85 kHz	96.1%	10 kW	ZVS and loss optimization at light loads, MEPT over wide load range
[63]	II	Yes	MSC, PSC	φ_r θ_r, K_t	IM, ZVS, CCO/CVO	85 kHz	93.9%	500 W	IM and ZVS under load variations
[65]	I	Yes	OOK	δ, K_t, K_r	IM, ZVS, CVO	200 kHz	94.761%	500 W	Low output DC voltage ripple
[89]	III	No	PDM	d_t, d_r, θ_t	IM, ZVS, CVO	0.917 MHz	72%	43.56 W	Simple implementation of ZVS over long distances
[90]	III	No	PDM	d_t, θ_t, θ_r	ZVS, CVO	102 kHz	80%	53.33 W	Monotonic output regulation
[92]	I	No	PDM	d_t, d_r	ZVS, CVO	0.909 MHz	85%	40.45 W	ZVS under large load and coupling variation
[66]	I	Yes	AVC, PSC, MSC	φ_t, φ_r, θ_r, K_t and K_r	IM, ZVS, CCO/CVO	85 kHz	96.85%	3.7 kW	ZVS and efficiency improvement under light and medium load conditions
[67]	I	Yes	APWMEN	φ_t, φ_r, δ and f_s	IM, ZVS	85 kHz 85/2 kHz	97.48%	1000 W	ZVS and efficiency improvement under light load conditions
[42]	II	Yes	OAC, DPSC	φ_t, φ_r	IM	85 kHz	90%	Not mentioned	Sensor-independent and fast MEPT
[72]	I	Yes	MPC, P&O, DPSC	φ_t, φ_r	Minimum DC current input, dynamic improvement	80 kHz	93.69%	Not mentioned	Improvement of the dynamic performance
[36]	I	Yes	MPC, P&O, DPSC	φ_t, φ_r	Minimum DC current input, dynamic improvement	85 kHz	94.8%	800 W	Improvement of the dynamic performance, sensor-independent
[74]	I	Yes	FLC, PDM	d_t, d_r	ZVS	85 kHz	93.1%	7 kW	ZVS and loss optimization under load variations
[75]	I	Yes	JAYA, PSC	φ_t, φ_r, f_s	Tuning impedance, parameter recognition	65–125 kHz	96%	800 W	Load-independent parameter recognition
[87]	I	No	P&O, DPSC	φ_t, φ_r	Minimum DC current input, CVO	101 kHz	79%	16 W	Eliminate communications while reduced size
[88]	II	No	P&O, DPSC	φ_t, φ_r	Minimum DC current input, CCO	85.5 kHz	81%	100 W	Compact receiver and no wireless communication
[76]	I	Yes	SCC, AVC, DPSC	φ_t, φ_r, α_t, α_r	IM, ZVS	100 kHz	91.2%	650 W	Tunable wide range soft-switching and efficiency optimization
[77]	II	Yes	SCC, DPSC	φ_t, φ_r, α_t	IM, ZVS, CVO	85 kHz	95.1%	6.6 kW	ZVS operation for reactive current minimization and total loss minimization
[78]	I	Yes	SCC, TPSC	φ_t, φ_r, δ and α_t	IM, ZVS	85 kHz	Not mentioned	6 kW	Wide output voltage variation range, ZVS for all switches
[79]	II	Yes	SCC, VFC, PSC	f_s, φ_r, α_r	IM, ZVS, CPO	82–114.8 kHz	93%	308 W	MEPT and power regulation under coupling and load variation, ZVS for all switches
[80]	II	Yes	VI, PSC	L_p, φ_r	ZVS, CCO	85 kHz	92.89%	974.1 W	ZVS for the whole charging process
[98]	II	No	VI	L_t, L_r	ZVS, CPO	85 kHz	92.5%	300 W	Good adjustability and high transmission efficiency over a wide range of misalignments
[99]	I	No	FOE, VFTPSC	φ_t, φ_r, θ_r and f_s	ZVS, CCO/CVO	208–220 kHz	95.1%	864 W	Constant output over wide range of misalignment and detuning

7. Key Issues and Development Trends

Based on the previous sections, we have understood the control methods of the DSC–MCWPT system based on the DAB converter. In this section, the key issues and development trends of this technology are given by combining the DSC methods from various papers and the problems in our study.

7.1. Key Issues

The research of DSC–MCWPT based on DAB converters has been paid more attention recently and various control methods have been continuously improved. Refs. [56,66,67,74] realizes bidirectional wireless energy transmission through DSC, which can realize both grid-to-load power supply, load-side feed to the grid, and can alleviate the problem of high grid load with loads stored in batteries. There are also papers that investigate EV charging [80] and supercapacitor charging [58], which to some extent can extend the battery range and service life, and can also fill the gaps of MCWPT in these areas. However, there are still some key issues to be solved to limit the efficiency, reliability, and practicability of the system. These key issues include:

1. Control complexity

Even though the basic compensation topology is used, the modeling process is more complicated for a dual-side controllable MCWPT system, which needs to consider the interrelationships of various control degrees of freedom. How to ensure that the various control loops are decoupled and minimize the complexity of the control strategy is a matter of practicality and portability.

2. Soft-switching loss

Soft-switching affects the efficiency and stability of the system. However, achieving soft-switching may lead to an increase in reactive power loss, resulting in a narrowing of the Impedance Matching range and a reduction in the power transfer capability. How the DSC strategy analyzes the conditions and influencing factors for the realization of soft-switching and how to optimize the loss under soft-switching are the problems that have been addressed by various control methods. In addition, most of the studies have focused only on ZVS turn-on without paying attention to the loss caused by ZCS turn-off.

3. Adjustment speed

The speed of regulation consists of the optimization of the efficiency and the constant output. The most direct reflection is the magnitude of the dynamic response time, but some articles do not have dynamic experiments or are insufficient. How the hardware and program are designed to ensure fast and efficient handling of sudden changes in load and coupling coefficients that will be encountered during real operation, as well as interference from wireless communication, are issues that must be considered in DSC.

4. Output accuracy

For practical power transmission needs, the constant output needs to satisfy a certain level of accuracy; therefore, maintaining a good output ripple while optimizing efficiency is one of the key issues. However, only a few articles have illustrated the amount of output variation and still lack analysis over the whole operating range.

5. Harmonic influence

Since the AC-measured voltage under the DAB structure is a square wave, although the coil current is highly sinusoidal at a high-quality factor, it can be analyzed by FHA. However, when the load and distance of the system change, the coil current may be distorted, affecting the accuracy of the control strategy calculation results. However, few articles have analyzed the control strategy affected by harmonics and the total harmonic distortion rate (THD) of voltage or current. In addition, to eliminate the wireless communication of the DSC, the scheme by estimating the load and output of the other side on one side needs to be concerned with the effect of harmonics.

6. Parameter drift

Since inductive coils usually use magnetic components to increase the coupling strength, variations in the transmission distance affect the self-inductance and thus the intrinsic resonant frequency of the system. The resonant capacitance also suffers from aging and tolerances. However, most DSC methods are based on resonant state analysis, and system detuning caused by parameter drift will undoubtedly degrade the performance of the control strategy. How to minimize the effect of the parameter drift of circuit components is one of the issues that has not been focused on yet.

7.2. Development Trends

Based on the above introduction, the following insights into the development trend of DSC–MCWPT based on DAB converter technology are provided:

1. Fast charging strategy

Although most DSC methods achieve constant output, it would be more meaningful for practical applications if various fast charging strategies could be combined and the efficiency-optimized control scheme could be improved accordingly.

2. Compact and simplified circuit structure

Utilizing the DAB converter and the basic compensation topology, choosing suitable power switches and resonant elements can further simplify the circuit structure of the system as a typical scheme. The design and improvement of the DSC strategy is then used as a renewal mode, which is expected to be one of the development trends of MCWPT.

3. Autonomous control strategy

The advantage of MCWPT is the freedom of power transmission, so it is inevitable that the system will deviate from its rated operating point, resulting in a degradation of transmission performance. If the output of the system can be made time-variable-free, it also means that the system is autonomous. Autonomous control strategy is one of the future trends as a scheme to counteract the variation of distance, and load and component parameters can improve the robustness of the system and prolong the service life of the product.

4. Dynamic wireless power transfer

Today, most of the MCWPT systems are only suitable for quasi-static wireless power transmission. With the high control freedom of DSC, it can provide a solution for practical dynamic wireless charging in reality, which can further improve the industrial application of MCWPT. How to establish the dynamic model of the system and realize dynamic wireless charging is the trend of future development.

5. Combination of magnetic technology and control strategies

Today, magnetic component design and loss optimization are becoming more sophisticated, improving the efficiency of many power converters. Current DSC strategies based on DAB converter focus on control design, which, if combined with magnetic technology to optimize the inductance, will lead to even higher efficiency and power density research results in the future.

8. Conclusions

The DSC–MCWPT technology based on DAB converters has a simplified circuit structure, systematic control scheme, and plays a key role in facilitating fast energy exchange between the grid and power-consuming devices. With the continuous development of DSC methods, more diverse control strategies and application scenarios are expected to emerge in the future.

This review begins with an introduction to bridge converters commonly used in DSC in Section 2, where three combinations of DAB converter topologies are summarized and

compared. Then, in Section 3, the key PSC technique of the bridge converter is introduced, the equivalent circuit of the system is analyzed using FHA, and the theory is linked to the DSC method by deriving the operating conditions for realizing IM and ZVS. The availability of wireless communication is used as an important factor to classify DSC, and there are more DSC strategies with communication in Section 4, most of which are based on PSC and other control methods to achieve efficiency optimization and constant output. Non-communicational DSC methods are less studied in Section 5, and although most of the control strategies are offset-resistant, further optimization of efficiency and dynamics is needed. In Section 6, a simple comparison of the control, transmission performance, and advantages is made based on wireless communication and non-communication DSC strategies together. Finally, in Section 7, insights are given on the key issues and trends in conjunction with existing methods.

Author Contributions: Conceptualization, Y.J. and Y.L.; methodology, Y.J. and Y.L.; validation, X.S., Y.L. and J.Y.; formal analysis, Y.J. and Y.L.; resources, Y.J. and Y.L.; writing—original draft preparation, Y.L.; writing—review and editing, Y.L. and X.S.; supervision, Y.J. and X.S.; project administration, Y.J., J.Y., and X.S.; funding acquisition, Y.J., J.Y., and X.S. All authors have read and agreed to the published version of the manuscript.

Funding: This work was supported by the National Natural Science Foundation of China under Grant 62201153; the National Natural Science Foundation of China under Grant 52207193; and the Natural Science Foundation of Fujian Province, China, under Grant 2023J01264.

Data Availability Statement: The data presented in this study are available upon request from the corresponding authors.

Conflicts of Interest: The authors declare no conflicts of interest.

Abbreviations

AR	Active Rectifier
AMC	Auxiliary Measurement Coil
ASPR	Active Single-Phase Rectifier
AVC	Asymmetrical Voltage Cancellation
CCO	Constant Current Output
CPO	Constant Power Output
CVO	Constant Voltage Output
CTM	Chain Triggered Mode
DAB	Dual-Active Bridge
DPSC	Dual-Phase Shift Control
DSC	Dual-Side Control
DSM	Delta–Sigma Modulator
EMI	Electromagnetic Interference
ESO	Expanded State Observer
EV	Electric Vehicle
FB	Full-Bridge
FHA	Fundamental Harmonic Approximation
FCS	Finite-Control-Set
FLC	Fuzzy Logic Control
FMPSK	Frequency-Modulated Phase-Shift Keying
FOE	Fractional Order Element
HB	Half-Bridge
IM	Impedance Matching
LM	Load Matching
MB	Mixed-Bridge
MC	Mode Changing
MCWPT	Magnetic Coupling Wireless Power Transfer
MEPT	Maximum Efficiency Point Tracking

MPC	Model Predictive Control
MSC	Mode-Switching Control
OAC	Optimal Algorithm Control
OMC	Optimal Efficiency Curve
OOK	On-Off Keying
PDM	Pulse Density Modulation
PFC	Power Factor Correction
PLL	Phase-Locked Loop
PSC	Phase-Shift Control
PSK	Phase-Shift Keying
PWM	Pulse Width Modulation
P&O	Perturbation and Observation
RF	Radio Frequency
RSC	Receiver-Side Control
SCC	Switch-Controlled Capacitor
SSC	Single-Side Control
SBAR	Semi-Bridgeless Active Rectifier
TPSC	Three Phase Shift Control
TSC	Transmitter-Side Control
UAV	Unmanned Aerial Vehicle
VFC	Variable Frequency Control
VFTPSC	Variable-Frequency Three Phase Shift Control
VI	Variable Inductor
ZCD	Zero-Crossing Detection
ZOM	Zero Output Mode
ZPA	Zero Phase Angle
ZVS	Zero-Voltage Switching

References

1. Marincic, A.S. Nikola Tesla and the Wireless Transmission of Energy. *IEEE Trans. Power Appar. Syst.* **1982**, *PAS-101*, 4064–4068. [CrossRef]
2. Cannon, B.L.; Hoburg, J.F.; Stancil, D.D.; Goldstein, S.C. Magnetic Resonant Coupling As a Potential Means for Wireless Power Transfer to Multiple Small Receivers. *IEEE Trans. Power Electron.* **2009**, *24*, 1819–1825. [CrossRef]
3. Hui, S.Y.R. Magnetic Resonance for Wireless Power Transfer [A Look Back]. *IEEE Power Electron. Mag.* **2016**, *3*, 14–31. [CrossRef]
4. Lu, F.; Zhang, H.; Mi, C. A Two-Plate Capacitive Wireless Power Transfer System for Electric Vehicle Charging Applications. *IEEE Trans. Power Electron.* **2018**, *33*, 964–969. [CrossRef]
5. Yang, L.; Ju, M.; Zhang, B. Bidirectional Undersea Capacitive Wireless Power Transfer System. *IEEE Access* **2019**, *7*, 121046–121054. [CrossRef]
6. Strassner, B.; Chang, K. Microwave Power Transmission: Historical Milestones and System Components. *Proc. IEEE* **2013**, *101*, 1379–1396. [CrossRef]
7. Liu, Q.; Wu, J.; Xia, P.; Zhao, S.; Chen, W.; Yang, Y.; Hanzo, L. Charging Unplugged: Will Distributed Laser Charging for Mobile Wireless Power Transfer Work? *IEEE Veh. Technol. Mag.* **2016**, *11*, 36–45. [CrossRef]
8. Denisov, A.; Yeatman, E. Ultrasonic vs. Inductive Power Delivery for Miniature Biomedical Implants. In Proceedings of the 2010 International Conference on Body Sensor Networks, Singapore, 7–9 June 2010; pp. 84–89.
9. Wang, C.-S.; Stielau, O.H.; Covic, G.A. Design Considerations for a Contactless Electric Vehicle Battery Charger. *IEEE Trans. Ind. Electron.* **2005**, *52*, 1308–1314. [CrossRef]
10. Hori, Y. Novel EV Society Based on Motor/Capacitor/Wireless—Application of Electric Motor, Supercapacitors, and Wireless Power Transfer to Enhance Operation of Future Vehicles. In Proceedings of the 2012 IEEE MTT-S International Microwave Workshop Series on Innovative Wireless Power Transmission: Technologies, Systems, and Applications, Kyoto, Japan, 10–11 May 2012; pp. 3–8.
11. Hui, S.Y. Planar Wireless Charging Technology for Portable Electronic Products and Qi. *Proc. IEEE* **2013**, *101*, 1290–1301. [CrossRef]
12. Jegadeesan, R.; Guo, Y.X.; Je, M. Electric Near-Field Coupling for Wireless Power Transfer in Biomedical Applications. In Proceedings of the 2013 IEEE MTT-S International Microwave Workshop Series on RF and Wireless Technologies for Biomedical and Healthcare Applications (IMWS-BIO), Singapore, 9–11 December 2013; pp. 1–3.
13. Si, P.; Hu, A.P.; Malpas, S.; Budgett, D. A Frequency Control Method for Regulating Wireless Power to Implantable Devices. *IEEE Trans. Biomed. Circuits Syst.* **2008**, *2*, 22–29. [CrossRef]
14. Dai, X.; Wu, J.; Jiang, J.; Gao, R.; Madawala, U.K. An Energy Injection Method to Improve Power Transfer Capability of Bidirectional WPT System with Multiple Pickups. *IEEE Trans. Power Electron.* **2021**, *36*, 5095–5107. [CrossRef]

15. Borage, M.; Tiwari, S.; Kotaiah, S. Analysis and Design of an LCL-T Resonant Converter as a Constant-Current Power Supply. *IEEE Trans. Ind. Electron.* **2005**, *52*, 1547–1554. [CrossRef]
16. Li, W.; Zhao, H.; Deng, J.; Li, S.; Mi, C.C. Comparison Study on SS and Double-Sided LCC Compensation Topologies for EV/PHEV Wireless Chargers. *IEEE Trans. Veh. Technol.* **2016**, *65*, 4429–4439. [CrossRef]
17. Feng, J.; Wei, G.; Zhang, J.; Zhu, C. An LCCC-LCC Compensated Dual-Coupled WPT System with MI Enhancement and High Misalignment Tolerance. *IEEE Trans. Power Electron.* **2023**, *38*, 15162–15167. [CrossRef]
18. Qu, X.; Han, H.; Wong, S.-C.; Tse, C.K.; Chen, W. Hybrid IPT Topologies with Constant Current or Constant Voltage Output for Battery Charging Applications. *IEEE Trans. Power Electron.* **2015**, *30*, 6329–6337. [CrossRef]
19. Chen, C.; Zhou, H.; Deng, Q.; Hu, W.; Yu, Y.; Lu, X.; Lai, J. Modeling and Decoupled Control of Inductive Power Transfer to Implement Constant Current/Voltage Charging and ZVS Operating for Electric Vehicles. *IEEE Access* **2018**, *6*, 59917–59928. [CrossRef]
20. Liu, F.; Chen, K.; Zhao, Z.; Li, K.; Yuan, L. Transmitter-Side Control of Both the CC and CV Modes for the Wireless EV Charging System with the Weak Communication. *IEEE J. Emerg. Sel. Top. Power Electron.* **2018**, *6*, 955–965. [CrossRef]
21. Song, K.; Li, Z.; Jiang, J.; Zhu, C. Constant Current/Voltage Charging Operation for Series–Series and Series–Parallel Compensated Wireless Power Transfer Systems Employing Primary-Side Controller. *IEEE Trans. Power Electron.* **2018**, *33*, 8065–8080. [CrossRef]
22. Li, Z.; Zhu, C.; Jiang, J.; Song, K.; Wei, G. A 3-kW Wireless Power Transfer System for Sightseeing Car Supercapacitor Charge. *IEEE Trans. Power Electron.* **2017**, *32*, 3301–3316. [CrossRef]
23. Fan, M.; Shi, L.; Yin, Z.; Li, Y. A Novel Pulse Density Modulation with Semi-Bridgeless Active Rectifier in Inductive Power Transfer System for Rail Vehicle. *CES Trans. Electr. Mach. Syst.* **2017**, *1*, 397–404. [CrossRef]
24. Lee, S.-H.; Lorenz, R.D. Development and Validation of Model for 95%-Efficiency 220-W Wireless Power Transfer Over a 30-Cm Air Gap. *IEEE Trans. Ind. Appl.* **2011**, *47*, 2495–2504. [CrossRef]
25. Beh, T.C.; Kato, M.; Imura, T.; Oh, S.; Hori, Y. Automated Impedance Matching System for Robust Wireless Power Transfer via Magnetic Resonance Coupling. *IEEE Trans. Ind. Electron.* **2013**, *60*, 3689–3698. [CrossRef]
26. Lim, Y.; Tang, H.; Lim, S.; Park, J. An Adaptive Impedance-Matching Network Based on a Novel Capacitor Matrix for Wireless Power Transfer. *IEEE Trans. Power Electron.* **2014**, *29*, 4403–4413. [CrossRef]
27. Zhong, W.; Hui, S.Y.R. Charging Time Control of Wireless Power Transfer Systems Without Using Mutual Coupling Information and Wireless Communication System. *IEEE Trans. Ind. Electron.* **2017**, *64*, 228–235. [CrossRef]
28. Kim, N.Y. Adaptive Magnetic Resonance Wireless Power Transfer System with Optimum Frequency and Power-Leve Tracking for Maintaining Highly Efficient. In Proceedings of the 2019 International Conference on Artificial Intelligence in Information and Communication (ICAIIC), Okinawa, Japan, 11–13 February 2019; pp. 543–547.
29. Colak, K.; Asa, E.; Bojarski, M.; Czarkowski, D.; Onar, O.C. A Novel Phase-Shift Control of Semibridgeless Active Rectifier for Wireless Power Transfer. *IEEE Trans. Power Electron.* **2015**, *30*, 6288–6297. [CrossRef]
30. Liu, Y.; Madawala, U.K.; Mai, R.; He, Z. Zero-Phase-Angle Controlled Bidirectional Wireless EV Charging Systems for Large Coil Misalignments. *IEEE Trans. Power Electron.* **2020**, *35*, 5343–5353. [CrossRef]
31. Song, J.; Yang, F.; Guo, Z.; Wu, X.; Zhu, K.; Jiang, J.; Sun, Y.; Li, Y.; Jiang, H.; Chen, H. Wireless Power Transfer via Topological Modes in Dimer Chains. *Phys. Rev. Appl.* **2021**, *15*, 014009. [CrossRef]
32. Ouddah, N.; Boukhnifer, M.; Chaibet, A.; Monmasson, E. Robust Controller Designs of Switched Reluctance Motor for Electrical Vehicle. In Proceedings of the 22nd Mediterranean Conference on Control and Automation, Palermo, Italy, 16–19 June 2014; pp. 212–217.
33. Zhu, H.; Zhang, B.; Wu, L. Output Power Stabilization for Wireless Power Transfer System Employing Primary-Side-Only Control. *IEEE Access* **2020**, *8*, 63735–63747. [CrossRef]
34. Assawaworrarit, S.; Yu, X.; Fan, S. Robust Wireless Power Transfer Using a Nonlinear Parity–Time-Symmetric Circuit. *Nature* **2017**, *546*, 387–390. [CrossRef]
35. Wang, C.; Wang, H. Research on Output Power Stability Control Method of EV-DWPT System. *Electr. Eng.* **2022**, *104*, 1247–1254. [CrossRef]
36. Chen, S.; Ding, W.; Huo, L.; Wu, X.; Shi, S.; Hu, R. Dynamic Improvement and Efficiency Optimization of Wireless Power Transfer Systems Using Improved FCS-MPC and P&O Methods. *IEEE Trans. Power Electron.* **2023**, *38*, 14702–14718.
37. Li, K.; Tan, S.-C. A Class E2 Inverter-Rectifier-Based Bidirectional Wireless Power Transfer System. In Proceedings of the 2018 IEEE 4th Southern Power Electronics Conference (SPEC), Singapore, 10–13 December 2018; pp. 1–6.
38. Wang, L.; Madawala, U.K.; Zhang, J.; Wong, M.-C. A New Bidirectional Wireless Power Transfer Topology. *IEEE Trans. Ind. Appl.* **2022**, *58*, 1146–1156. [CrossRef]
39. Kalra, G.R.; Thrimawithana, D.J.; Riar, B.S.; Huang, C.-Y.; Neuburger, M. A Novel Boost Active Bridge-Based Inductive Power Transfer System. *IEEE Trans. Ind. Electron.* **2020**, *67*, 1103–1112. [CrossRef]
40. Zhang, Y.; Chen, S.; Li, X.; Tang, Y. Dual-Side Phase-Shift Control of Wireless Power Transfer Implemented on Primary Side Based on Driving Windings. *IEEE Trans. Ind. Electron.* **2021**, *68*, 8999–9002. [CrossRef]
41. Zhang, Z.; Pang, H.; Georgiadis, A.; Cecati, C. Wireless Power Transfer—An Overview. *IEEE Trans. Ind. Electron.* **2019**, *66*, 1044–1058. [CrossRef]
42. Yang, L.; Shi, Y.; Wang, M.; Ren, L. Constant Voltage Charging and Maximum Efficiency Tracking for WPT Systems Employing Dual-Side Control Scheme. *IEEE J. Emerg. Sel. Top. Power Electron.* **2022**, *10*, 945–955. [CrossRef]

43. Berger, A.; Agostinelli, M.; Vesti, S.; Oliver, J.A.; Cobos, J.A.; Huemer, M. A Wireless Charging System Applying Phase-Shift and Amplitude Control to Maximize Efficiency and Extractable Power. *IEEE Trans. Power Electron.* **2015**, *30*, 6338–6348. [CrossRef]
44. Li, M.; Deng, J.; Chen, D.; Wang, W.; Wang, Z. Maximum Efficiency Tracking and ZVS Realization for Wide Output Voltage Range Employing Segmented TPS Modulation Scheme. *IEEE Trans. Veh. Technol.* **2023**, *72*, 12770–12783. [CrossRef]
45. Li, Y.; Hu, J.; Chen, F.; Li, Z.; He, Z.; Mai, R. Dual-Phase-Shift Control Scheme with Current-Stress and Efficiency Optimization for Wireless Power Transfer Systems. *IEEE Trans. Circuits Syst. I Regul. Pap.* **2018**, *65*, 3110–3121. [CrossRef]
46. Jiang, Y.; Wang, L.; Wang, Y.; Wu, M.; Zeng, Z.; Liu, Y.; Sun, J. Phase-Locked Loop Combined with Chained Trigger Mode Used for Impedance Matching in Wireless High Power Transfer. *IEEE Trans. Power Electron.* **2020**, *35*, 4272–4285. [CrossRef]
47. Wang, S.; Jiang, C.; Lu, Q.; Xia, C.; Wei, N. Research on Synchronous Phase Shift Control Strategy of Bilateral Converter in Bidirectional Inductive Power Transfer System. *J. Electr. Eng. Technol.* **2021**, *16*, 2485–2495. [CrossRef]
48. Moghaddam, M.F.; Vaez-Zadeh, S.; Zakerian, A.; Babaki, A. Design and Analysis of a Modified Dual Phase Shift Control Method for a Wireless EV Charger Considering Coupling Uncertainty. In Proceedings of the 2019 10th International Power Electronics, Drive Systems and Technologies Conference (PEDSTC), Shiraz, Iran, 12–14 February 2019; pp. 635–640.
49. Nguyen, B.X.; Vilathgamuwa, D.M.; Foo, G.H.B.; Wang, P.; Ong, A.; Madawala, U.K.; Nguyen, T.D. An Efficiency Optimization Scheme for Bidirectional Inductive Power Transfer Systems. *IEEE Trans. Power Electron.* **2015**, *30*, 6310–6319. [CrossRef]
50. Zhang, X.; Cai, T.; Duan, S.; Feng, H.; Hu, H.; Niu, J.; Chen, C. A Control Strategy for Efficiency Optimization and Wide ZVS Operation Range in Bidirectional Inductive Power Transfer System. *IEEE Trans. Ind. Electron.* **2019**, *66*, 5958–5969. [CrossRef]
51. Xu, F.; Wong, S.-C.; Tse, C.K. Overall Loss Compensation and Optimization Control in Single-Stage Inductive Power Transfer Converter Delivering Constant Power. *IEEE Trans. Power Electron.* **2022**, *37*, 1146–1158. [CrossRef]
52. Jiang, Y.; Wang, L.; Fang, J.; Zhao, C.; Wang, K.; Wang, Y. A Joint Control with Variable ZVS Angles for Dynamic Efficiency Optimization in Wireless Power Transfer System. *IEEE Trans. Power Electron.* **2020**, *35*, 11064–11081. [CrossRef]
53. Mai, R.; Liu, Y.; Li, Y.; Yue, P.; Cao, G.; He, Z. An Active-Rectifier-Based Maximum Efficiency Tracking Method Using an Additional Measurement Coil for Wireless Power Transfer. *IEEE Trans. Power Electron.* **2018**, *33*, 716–728. [CrossRef]
54. Liu, Y.; Madawala, U.K.; Mai, R.; He, Z. An Optimal Multivariable Control Strategy for Inductive Power Transfer Systems to Improve Efficiency. *IEEE Trans. Power Electron.* **2020**, *35*, 8998–9010. [CrossRef]
55. Dong, W.; Madawala, U.K.; Baguley, C.A. Optimal Control of LCL Tuned Inductive Power Transfer (IPT) Systems Using All Control Variables. *IEEE Trans. Transp. Electrif.* **2024**, *10*, 4347–4358. [CrossRef]
56. Huang, J.; He, X.; Huo, P.; Xu, R. A Hybrid Modulation Strategy for LCC–LCC Compensated Bidirectional Wireless Power Transfer System to Achieve High Efficiency in the Whole Operating Range. *IEEE Trans. Ind. Electron.* **2024**, *71*, 327–337. [CrossRef]
57. Song, K.; Yang, G.; Zhang, H.; Huang, X.; Jiang, J.; Lan, Y.; Huang, X.; Li, J.; Zhu, C. An Impedance Decoupling-Based Tuning Scheme for Wireless Power Transfer System Under Dual-Side Capacitance Drift. *IEEE Trans. Power Electron.* **2021**, *36*, 7526–7536. [CrossRef]
58. Huang, Z.; Wang, D.; Qu, X. A Novel IPT Converter with Current-Controlled Semi-Active Rectifier for Efficiency Enhancement Throughout Supercapacitor Charging Process. *IEEE J. Emerg. Sel. Top. Power Electron.* **2022**, *10*, 2201–2209. [CrossRef]
59. Chen, S.; Chen, Y.; Li, H.; Dung, N.A.; Mai, R.; Tang, Y.; Lai, J.-S. An Operation Mode Selection Method of Dual-Side Bridge Converters for Efficiency Optimization in Inductive Power Transfer. *IEEE Trans. Power Electron.* **2020**, *35*, 9992–9997. [CrossRef]
60. Fan, Z.; Wang, F.; Yang, J. Half-Bridge Modulation Strategy for Bidirectional Wireless Power Transfer Based on Efficiency Optimization Under Light Load Conditions. In Proceedings of the 3rd International Symposium on New Energy and Electrical Technology, Anyang, China, 25–27 August 2022; Cao, W., Hu, C., Chen, X., Eds.; Springer: Singapore, 2023; Volume 1017, pp. 621–628.
61. Li, Y.; Sun, W.; Zhu, X.; Hu, J. A Hybrid Modulation Control for Wireless Power Transfer Systems to Improve Efficiency Under Light-Load Conditions. *IEEE Trans. Ind. Electron.* **2022**, *69*, 6870–6880. [CrossRef]
62. Zhu, G.; Dong, J.; Shi, W.; Soeiro, T.B.; Xu, J.; Bauer, P. A Mode-Switching-Based Phase Shift Control for Optimized Efficiency and Wide ZVS Operations in Wireless Power Transfer Systems. *IEEE Trans. Power Electron.* **2023**, *38*, 5561–5575. [CrossRef]
63. Wu, M.; Yang, X.; Chen, W.; Wang, L.; Jiang, Y.; Zhao, C.; Yan, Z. A Dual-Sided Control Strategy Based on Mode Switching for Efficiency Optimization in Wireless Power Transfer System. *IEEE Trans. Power Electron.* **2021**, *36*, 8835–8848. [CrossRef]
64. Zhong, W.; Hui, S.Y.R. Maximum Energy Efficiency Operation of Series-Series Resonant Wireless Power Transfer Systems Using On-Off Keying Modulation. *IEEE Trans. Power Electron.* **2018**, *33*, 3595–3603. [CrossRef]
65. Li, Y.; Cui, X.; Chen, J.; Liu, Y.; Liu, S.; Hu, J.; He, Z. Enhanced On-Off Keying Modulation for Wireless Power Transfer Systems to Improve Efficiency Over a Wide Load Range. *IEEE Trans. Veh. Technol.* **2024**, *73*, 6409–6419. [CrossRef]
66. Jia, S.; Chen, C.; Duan, S.; Chao, Z. Dual-Side Asymmetrical Voltage-Cancelation Control for Bidirectional Inductive Power Transfer Systems. *IEEE Trans. Ind. Electron.* **2021**, *68*, 8061–8071. [CrossRef]
67. Jiang, M.; Chen, C.; Jia, S.; Chen, H. An Asymmetrical Pulsewidth Modulation with Even Harmonics for Bidirectional Inductive Power Transfer Under Light Load Conditions. *IEEE Trans. Ind. Electron.* **2022**, *69*, 8939–8948. [CrossRef]
68. Li, H.; Li, J.; Wang, K.; Chen, W.; Yang, X. A Maximum Efficiency Point Tracking Control Scheme for Wireless Power Transfer Systems Using Magnetic Resonant Coupling. *IEEE Trans. Power Electron.* **2015**, *30*, 3998–4008. [CrossRef]
69. Dai, X.; Li, X.; Li, Y.; Hu, A.P. Maximum Efficiency Tracking for Wireless Power Transfer Systems with Dynamic Coupling Coefficient Estimation. *IEEE Trans. Power Electron.* **2018**, *33*, 5005–5015. [CrossRef]

70. Yeo, T.-D.; Kwon, D.; Khang, S.-T.; Yu, J.-W. Design of Maximum Efficiency Tracking Control Scheme for Closed-Loop Wireless Power Charging System Employing Series Resonant Tank. *IEEE Trans. Power Electron.* **2017**, *32*, 471–478. [CrossRef]
71. Liu, F.; Li, K.; Chen, K.; Zhao, Z. A Phase Synchronization Technique Based on Perturbation and Observation for Bidirectional Wireless Power Transfer System. *IEEE J. Emerg. Sel. Top. Power Electron.* **2020**, *8*, 1287–1297. [CrossRef]
72. Liu, S.; Mai, R.; Zhou, L.; Li, Y.; Hu, J.; He, Z.; Yan, Z.; Wang, S. Dynamic Improvement of Inductive Power Transfer Systems with Maximum Energy Efficiency Tracking Using Model Predictive Control: Analysis and Experimental Verification. *IEEE Trans. Power Electron.* **2020**, *35*, 12752–12764. [CrossRef]
73. Chen, S.; Ding, W. A Novel Finite-Control-Set Model Predictive Voltage Control for Dynamic Improvement of Wireless Power Transfer Systems. In Proceedings of the 2021 IEEE 4th International Electrical and Energy Conference (CIEEC), Wuhan, China, 28–30 May 2021; pp. 1–6.
74. Venkatesan, M.; Narayanamoorthi, R.; Emara, A.; Ghadi, Y.Y. Fuzzy Logic Controlled Pulse Density Modulation Technique for Bidirectional Inductive Power Transfer Systems. *IEEE Access* **2024**, *12*, 55184–55200. [CrossRef]
75. Zhu, G.; Dong, J.; Grazian, F.; Bauer, P. A Parameter Recognition-Based Impedance Tuning Method for SS-Compensated Wireless Power Transfer Systems. *IEEE Trans. Power Electron.* **2023**, *38*, 13298–13314. [CrossRef]
76. Zhang, J.; Zhao, J.; Zhang, Y.; Deng, F. A Wireless Power Transfer System with Dual Switch-Controlled Capacitors for Efficiency Optimization. *IEEE Trans. Power Electron.* **2020**, *35*, 6091–6101. [CrossRef]
77. Fu, N.; Deng, J.; Wang, Z.; Chen, D. Dual-Phase-Shift Control Strategy with Switch-Controlled Capacitor for Overall Efficiency Optimization in Wireless Power Transfer System. *IEEE Trans. Veh. Technol.* **2023**, *72*, 7304–7317. [CrossRef]
78. Zhang, R.; Deng, J.; Fu, N.; Wang, S.; Zhang, Z. Wide Range Output with Switch-Controlled Capacitor in Wireless Power Transfer System for Electric Vehicle Charging. In Proceedings of the 2023 IEEE International Future Energy Electronics Conference (IFEEC), Sydney, Australia, 20–23 November 2023; pp. 292–295.
79. Zou, B.; Huang, Z. Primary-Frequency-Tuning and Secondary-Impedance-Matching IPT Converter with Programmable Constant Power Output and Optimal Efficiency Tracking Against Variation of Coupling Coefficient. *IEEE Trans. Power Electron.* **2024**, *39*, 4895–4909. [CrossRef]
80. Iam, I.-W.; Ding, Z.; Ieong, C.-F.; Lam, C.-S.; Martins, R.P.; Mak, P.-I. Optimal Bivariate Control Strategy of Multistage Constant Current Charging for IPT-Based Wireless Electric Vehicle Charging. *IEEE Trans. Transp. Electrif.* **2024**, *10*, 4513–4528. [CrossRef]
81. Pashaei, A.; Aydin, E.; Aydemir, M.T. Dual Side Control Design for a 600W LCC Compensated Wireless Power Transfer System. In Proceedings of the 2022 Global Energy Conference (GEC), Batman, Turkey, 26–29 October 2022; pp. 80–83.
82. Sung, M.; Min, G.-H.; Ha, J.-I. Dual Side Control of Wireless Power Transfer with Mutual Inductance Estimation. In Proceedings of the 2020 IEEE Energy Conversion Congress and Exposition (ECCE), Detroit, MI, USA, 11–15 October 2020; pp. 1528–1533.
83. Iam, I.-W.; Hoi, I.-U.; Huang, Z.; Gong, C.; Lam, C.-S.; Mak, P.-I.; Martins, R.P.D.S. Constant-Frequency and Noncommunication-Based Inductive Power Transfer Converter for Battery Charging. *IEEE J. Emerg. Sel. Top. Power Electron.* **2022**, *10*, 2147–2162. [CrossRef]
84. Liu, F.; Lei, W.; Wang, T.; Nie, C.; Wang, Y. A Phase-Shift Soft-Switching Control Strategy for Dual Active Wireless Power Transfer System. In Proceedings of the 2017 IEEE Energy Conversion Congress and Exposition (ECCE), Cincinnati, OH, USA, 1–5 October 2017; pp. 2573–2578.
85. Placzek, J.M.; Beiranvand, H.; Liserre, M. Communicationless Phase Cooperative Control of Inductive Power Transfer Using Asymmetrical Modulations. *IEEE Trans. Power Electron.* **2023**, *38*, 7836–7847. [CrossRef]
86. Thrimawithana, D.J.; Madawala, U.K.; Neath, M. A Synchronization Technique for Bidirectional IPT Systems. *IEEE Trans. Ind. Electron.* **2013**, *60*, 301–309. [CrossRef]
87. Liu, X.; Wang, T.; Yang, X.; Tang, H. Analysis of Efficiency Improvement in Wireless Power Transfer System. *IET Power Electron.* **2018**, *11*, 302–309. [CrossRef]
88. Li, Z.; Song, K.; Jiang, J.; Zhu, C. Constant Current Charging and Maximum Efficiency Tracking Control Scheme for Supercapacitor Wireless Charging. *IEEE Trans. Power Electron.* **2018**, *33*, 9088–9100. [CrossRef]
89. Li, H.; Fang, J.; Chen, S.; Wang, K.; Tang, Y. Pulse Density Modulation for Maximum Efficiency Point Tracking of Wireless Power Transfer Systems. *IEEE Trans. Power Electron.* **2018**, *33*, 5492–5501. [CrossRef]
90. Chen, S.; Li, H.; Tang, Y. A Monotonic Output Regulation Method for Series-Series Compensated Inductive Power Transfer Systems with Improved Efficiency and Communication-Less Control. In Proceedings of the 2018 IEEE Energy Conversion Congress and Exposition (ECCE), Portland, OR, USA, 23–27 September 2018; pp. 6173–6178.
91. Dai, R.; Mai, R.; Zhou, W. A Pulse Density Modulation Based Receiver Reactance Identification Method for Wireless Power Transfer System. *IEEE Trans. Power Electron.* **2022**, *37*, 11394–11405. [CrossRef]
92. Li, H.; Wang, K.; Fang, J.; Tang, Y. Pulse Density Modulated ZVS Full-Bridge Converters for Wireless Power Transfer Systems. *IEEE Trans. Power Electron.* **2019**, *34*, 369–377. [CrossRef]
93. Li, H.; Chen, S.; Fang, J.; Tang, Y. Synchronous Rectification-Based Phase Shift Keying Communication for Wireless Power Transfer Systems. In Proceedings of the 2018 IEEE 4th Southern Power Electronics Conference (SPEC), Singapore, 10–13 December 2018; pp. 1–4.
94. Li, H.; Chen, S.; Fang, J.; Wang, K. Frequency-Modulated Phase Shift Keying Communication for MEPT Control of Wireless Power Transfer. *IEEE Trans. Power Electron.* **2021**, *36*, 4954–4959. [CrossRef]

95. Wang, C.; Fan, Y.; Gao, W.; Wang, K.; Li, H. PDM-Based Feedforward Power Compensation for FMPSK Communication in WPT Systems. *IEEE Trans. Circuits Syst. II Express Briefs* **2022**, *69*, 2241–2245. [CrossRef]
96. Yang, Y.; Tan, S.C.; Hui, S.Y.R. Fast Hardware Approach to Determining Mutual Coupling of Series–Series-Compensated Wireless Power Transfer Systems with Active Rectifiers. *IEEE Trans. Power Electron.* **2020**, *35*, 11026–11038. [CrossRef]
97. Wei, Y.; Chen, J.; Guo, J.; Li, H. Full-Duplex Frequency-Modulated Phase-Shift Keying Communication Method for Wireless Power Transfer System. *J. Power Supply* **2022**, *20*, 67–74.
98. Yenil, V. A Wireless Power Transfer System with High Misalignment Tolerance Based on Dual Side Variable Inductor Control. *IEEE Access* **2024**, *12*, 134937–134947. [CrossRef]
99. Rong, C.; Zhang, B. A Fractional-Order Wireless Power Transfer System with Misalignment and Detuning Tolerance. *IEEE Trans. Power Electron.* **2023**, *38*, 14884–14895. [CrossRef]

Disclaimer/Publisher's Note: The statements, opinions and data contained in all publications are solely those of the individual author(s) and contributor(s) and not of MDPI and/or the editor(s). MDPI and/or the editor(s) disclaim responsibility for any injury to people or property resulting from any ideas, methods, instructions or products referred to in the content.